

A Bayesian Non-parametric Approach to Generative Models: Integrating Variational Autoencoders and Generative Adversarial Networks using the Wasserstein Distance and Maximum Mean Discrepancy

Forough Fazeli-Asl

*Department of Statistics and Actuarial Science
University of Hong Kong
Pok Fu Lam, Hong Kong*

FOROUGHF@HKU.HK

Michael Minyi Zhang

*Department of Statistics and Actuarial Science
University of Hong Kong
Pok Fu Lam, Hong Kong*

MZHANG18@HKU.HK

Abstract

We propose a novel generative model within the Bayesian non-parametric learning (BNPL) framework to address some notable failure modes in generative adversarial networks (GANs) and variational autoencoders (VAEs)—these being overfitting in the GAN case and noisy samples in the VAE case. We will demonstrate that the BNPL framework enhances training stability and provides robustness and accuracy guarantees when incorporating the Wasserstein distance and maximum mean discrepancy measure (WMMD) into our model’s loss function. Moreover, we introduce a so-called “triple model” that combines the GAN, the VAE, and further incorporates a code-GAN (CGAN) to explore the latent space of the VAE. This triple model design generates high-quality, diverse samples, while the BNPL framework, leveraging the WMMD loss function, enhances training stability. Together, these components enable our model to achieve superior performance across various generative tasks. These claims are supported by both theoretical analyses and empirical validation on a wide variety of datasets.

Keywords: Bayesian non-parametrics, generative models, variational autoencoders.

1. Introduction

Generative modeling is a method to synthetically create new realistic data samples from an existing dataset. The original GAN, also known as Vanilla GAN, was introduced by Goodfellow et al. (2014), and since then, various types of adversarially trained generative models have been developed. These models have exhibited outstanding performance in creating sharp and realistic images by training two neural networks concurrently, one for generating images and the other for discriminating between authentic and counterfeit images. These networks are trained in an adversarial manner until the discriminator cannot distinguish between real and fake samples.

Despite GANs being a powerful class of deep-learning models, they still face some notable challenges including mode collapse and training instability. The mode collapse issue in GANs occurs when the generator starts to memorize the training data instead of learning

the underlying patterns of the data. This results in the generator becoming too specialized in generating the same samples repeatedly, which leads to a lack of diversity in the generated samples. Unlike GANs, VAEs use a probabilistic approach to encode and decode data, enabling them to learn the underlying distribution and generate diverse samples, albeit with some blurriness. Consequently, the integration of the GAN and the VAE has garnered attention as an intriguing idea for generating high-quality, realistic data samples. This approach allows for the full exploitation of the strengths of both generative models while mitigating their shortcomings.

Moreover, we can look at deep generative models from the perspective of frequentist and Bayesian methods in both its parametric and non-parametric forms. Parametric generative models assume a specific form for the data distribution, which can lead to overfitting (Ma et al., 2024; Mescheder et al., 2017). This occurs when the generator fits the training data too closely, limiting its ability to generalize to new data. The frequentist non-parametric (FNP) approach computes the loss function of a generative model with respect to the empirical data distribution, which assumes that the observed data are representative samples of the true population. However, especially with small sample sizes or complex data-generating mechanisms, the FNP approach can also contribute to overfitting, resulting in poor generalization and unstable out-of-sample performance, with the GAN becoming overly sensitive to minor data perturbations (Bariletto and Ho, 2024).

In contrast, BNP methods address overfitting in GANs by enabling the generator to adapt to the complexity of the data without adhering to a parametric distribution *a priori*. By avoiding overfitting, we can obtain more robust results in BNPL compared to its frequentist counterparts. However, developing a BNP procedure in training deep generative models remains a significant challenge because obtaining a posterior distribution for these models is intractable.

To address the aforementioned problems, we introduce a novel triple generative model that integrates a GAN, a VAE, and a code-GAN (CGAN) within the BNPL framework. The GAN functions as the primary component, while the VAE and CGAN enhance the model’s capabilities. Specifically, to generate more diverse samples, the GAN’s generator is replaced with the decoder of a VAE model. Additionally, an extra GAN is employed in the code space to generate supplementary sample codes. The CGAN complements the VAE by exploring underrepresented regions of the code space, promoting comprehensive coverage and mitigating mode collapse.

To fit this model within the framework of BNPL, we first develop a stochastic representation of the Wasserstein distance using the Dirichlet process (DP). This allows us to tractably estimate the Wasserstein distance between the DP posterior and the generator’s distribution, which is then incorporated into a DP-estimated MMD loss function. By minimizing both the Wasserstein distance and MMD as terms in the loss function of the triple model, our proposed BNPL model yields robustness during training. *In summary, our triple model enhances the quality, diversity, and visualization of the generated outputs, while the BNPL framework improves the training stability by enhancing out-of-sample performance, addresses model misspecification, and provides robustness guarantees against outliers, making it an excellent choice for high-quality image generation.*

The structure of the paper is organized as follows: In Section 2, we provide an overview of traditional learning approaches for generative models, including VAEs and GANs, compared

to the BNPL framework. Next, in Section 3, we introduce a probabilistic method to calculate the Wasserstein distance using a DP prior. Then, in Section 4, we introduce our triple generative model, a VAE-GAN calibrated with a CGAN, within the BNPL framework. Afterwards, in Section 5, we provide experimental results of our novel generative model. Lastly, we conclude our paper in Section 6 and provide some new directions based on the research presented in this paper. In the appendix, we provide key definitions to the WMMD metric, along with additional theoretical results on the accuracy and robustness grantees of the estimated generator parameters under our BNPL approach.

2. Background Work

We begin this section with a review of classic learning approaches to deep generative models from the frequentist perspective. Then, this section continues with an introduction to Bayesian non-parametric learning methods.

2.1 Deep Generative Modeling

2.1.1 VANILLA GAN

In the vanilla GAN, the generator tries to minimize the probability that the discriminator correctly identifies the fake sample, while the discriminator tries to maximize the probability of correctly identifying real and fake samples (Goodfellow et al., 2014). The GAN can be mathematically represented as a minimax game between the generator $\{Gen_{\omega}\}_{\omega \in \Omega}$, a family of neural network functions parameterized by ω within a compact domain $\Omega \subset \mathbb{R}^{t_1}$, which maps from the latent space \mathbb{R}^p to the data space \mathbb{R}^d , $p < d$, and a discriminator $\{Dis_{\theta}\}_{\theta \in \Theta}$, a family of neural network functions parameterized by θ within a compact domain $\Theta \subset \mathbb{R}^{t_2}$, which maps from the data space to the interval $[0, 1]$. Specifically, discriminator outputs represent how likely the generated sample is drawn from the true data distribution. For a real sample \mathbf{X} from a data distribution F , this can be expressed as the objective function

$$\arg \min_{\omega \in \Omega} \max_{\theta \in \Theta} \mathcal{L}(Gen_{\omega}, Dis_{\theta}),$$

where $\mathcal{L}(Gen_{\omega}, Dis_{\theta}) = E_F[\ln(Dis_{\theta}(\mathbf{X}))] + E_{F_{\mathbf{Z}_r}}[\ln(1 - Dis_{\theta}(Gen_{\omega}(\mathbf{Z}_r)))]$, $F_{\mathbf{Z}_r}$ is the distribution of the random noise vector \mathbf{Z}_r , and $\ln(\cdot)$ denotes the natural logarithm. Throughout the paper, it is assumed that $F_{\mathbf{Z}_r}$ follows a standard Gaussian distribution.

GANs are further extended by modifying the generator loss function, $\mathcal{L}_{Gen}(\omega)$, and discriminator loss function, $\mathcal{L}_{Dis}(\theta)$. To facilitate fair comparisons among different GAN models, we reformulate the vanilla GAN objective function as a sum of $\mathcal{L}_{Gen}(\omega)$ and $\mathcal{L}_{Dis}(\theta)$ by defining:

$$\mathcal{L}_{Gen}(\omega) = E_{F_{\mathbf{Z}_r}}[\ln(1 - Dis_{\theta}(Gen_{\omega}(\mathbf{Z}_r)))] \tag{1}$$

$$\mathcal{L}_{Dis}(\theta) = -E_F[\ln(Dis_{\theta}(\mathbf{X}))] - E_{F_{\mathbf{Z}_r}}[\ln(1 - Dis_{\theta}(Gen_{\omega}(\mathbf{Z}_r)))] \tag{2}$$

Now, the vanilla GAN is trained by iteratively updating ω and θ using stochastic gradient descent to minimize the loss functions (1) and (2), respectively. The training procedure for the GAN is finished when the generator can produce samples that are indistinguishable from the real samples, and the discriminator cannot differentiate between them.

2.1.2 MODE COLLAPSE IN GANS

Instability in GANs occurs when the generator and the discriminator are incapable of converging to a stable equilibrium (Kodali et al., 2017). A significant factor contributing to these issues is the tendency of the gradients used to update network parameters to become exceedingly small during the training process, causing the vanishing gradient that leads to a slowdown or even prevention of learning (Arjovsky and Bottou, 2017).

To mitigate mode collapse and enhance the stability property in GANs, Salimans et al. (2016) proposed using a batch normalization technique to normalize the output of each generator layer, which can help reduce the impact of vanishing gradients. The authors also implemented mini-batch discrimination, an additional technique to diversify the generated output. This involves computing a pairwise distance matrix among examples within a mini-batch. This matrix is then used to augment the input data before being fed into the model.

Another strategy, widely suggested in the literature to overcome GAN limitations, is incorporating statistical distances into the GAN loss function. Arjovsky et al. (2017) suggested updating GAN parameters by minimizing the Wasserstein distance between the distribution of the real and fake data (WGAN). They noted that this distance possesses a superior property compared to other metrics and measures like Kulback-Leibler, Jensen-Shannon, and total variation measures. This is due to its ability to serve as a sensible loss function for learning distributions supported by low-dimensional manifolds. Arjovsky et al. (2017) used the weight clipping technique to constrain the discriminator to the 1-Lipschitz constant. This condition ensures discriminator’s weights are bounded to prevent the discriminator from becoming too powerful and overwhelming the generator. Additionally, this technique helped to ensure that the gradients of the discriminator remained bounded, which is crucial for the stability of the overall training process.

However, weight clipping has some drawbacks. For instance, Gulrajani et al. (2017) noted that it may limit the capacity of the discriminator, which can prevent it from learning complex functions. Moreover, it can result in a “dead zone” where some of the discriminator’s outputs are not used, which can lead to inefficiencies in training. To address these issues, Gulrajani et al. (2017) proposed to force the 1-Lipschitz constraint on the discriminator in an alternative way. They improved WGAN using a gradient penalty term in the loss function to present the WGPAN model. They showed that it helps to avoid mode collapse and makes the training process more stable.

Instead of comparing the overall distribution of the data and the generator, Salimans et al. (2016) remarked on adopting the feature matching technique as a stronger method to prevent the mode collapse in GANs and make them more stable. In this strategy, the discriminator is a feature matching distance and the generator is trained to deceive the discriminator by producing images that match the features of real images, rather than just assessing the overall distribution of the data.

2.1.3 GENERATIVE MOMENT MATCHING NETWORKS

Dziugaite et al. (2015) and Li et al. (2015) independently proposed the similar techniques, which demonstrated impressive results by applying the MMD measure within a simple GAN framework. Li et al. (2015) referred to this technique as Generative Moment Matching

Networks (GMMNs). Previous work in GMMNs has used the MMD as a loss function to train both the generators to match the fake and real samples, as well as to train the latent space embeddings.

Embedding in the data space: Dziugaite et al. (2015) considered the loss function (3) to train the generator:

$$\arg \min_{\omega \in \Omega} \text{MMD}^2(F, F_{Gen_\omega}). \quad (3)$$

However, Li et al. (2015) mentioned that by incorporating the square root of the MMD measure into the GAN loss function, the gradients used to update the generator can be more stable, preventing them from becoming too small and leading to gradient vanishing.

Embedding in the latent space: Li et al. (2015) applied the GMMN concept in the code space of an autoencoder (AE+GMMNs) to propose a bootstrap autoencoder model. The training procedure for this model begins with greedy layer-wise pretraining of the autoencoder (Bengio et al., 2006), where each layer is trained individually in an unsupervised manner to compress data into a lower-dimensional representation (code space) that captures the essential features of the original data. This compressed representation is then used to reconstruct (or decode) the original input. After the pretraining phase, the auto-encoder is fine-tuned using backpropagation to improve its reconstruction performance. Once the auto-encoder is fully trained, its weights are frozen, and a GMMN is trained to model the distribution of the code layer.

The GMMN generator, which is fed with sub-latent noise, generates codes in the code space. The objective is to minimize the MMD between the generated codes and the real data codes, optimizing the GMMN objective on the final encoding layer of the auto-encoder. Li et al. (2015) demonstrated that this approach significantly reduced noise in the decoded samples. However, since it does not model the latent space probabilistically, it cannot sample or generate novel data points beyond those already seen during the bootstrap procedure.

2.1.4 STANDARD VAE

The VAE consists of an encoder $\{Enc_\eta\}_{\eta \in \mathfrak{S}}$, a family of neural network functions parameterized by η within a compact domain $\mathfrak{S} \subset \mathbb{R}^{s_1}$, which maps the input data $\mathbf{X} \sim F$ to a latent representation \mathbf{Z}_e , and a decoder $\{Dec_\gamma\}_{\gamma \in \Gamma}$, a family of neural network functions parameterized by γ within a compact domain $\Gamma \subset \mathbb{R}^{s_2}$, which reconstructs \mathbf{Z}_e back to the data space (Kingma and Welling, 2013). It uses a hierarchical distribution to model the underlying distribution of the data. Precisely, a prior distribution $F_{\mathbf{Z}_r}$ is first placed on the latent space, $\mathbf{Z}_r \sim F_{\mathbf{Z}_r}$, to specify the distribution of the encoder (variational distribution), $\mathbf{Z}_e := \mathbf{Z}_r | \mathbf{X} \sim F_{Enc_\eta}$, and the distribution of the decoder, $\mathbf{X} | \mathbf{Z}_r \sim F_{Dec_\gamma}$, by the reparametrization trick. Then, the intractable data likelihood is approximated by maximizing the marginal log-likelihood:

$$\ln f_{Dec_\gamma}(\mathbf{x}) = \ln \int f_{Dec_\gamma}(\mathbf{x} | \mathbf{z}_r) f_{\mathbf{Z}_r}(\mathbf{z}_r) d\mathbf{z}_r, \quad (4)$$

where f_{Dec_γ} represents the density function corresponding to F_{Dec_γ} . It can be shown that maximizing (4) is equivalent to minimizing:

$$\begin{aligned} \mathcal{L}_{VAE}(\boldsymbol{\eta}, \boldsymbol{\gamma}) &= \text{KL}(f_{Enc_\eta}(\mathbf{z}_r|\mathbf{x}), f_{\mathbf{z}_r}(\mathbf{z}_r)) - E_{F_{Enc_\eta}(\mathbf{z}_r|\mathbf{x})}(\ln f_{Dec_\gamma}(\mathbf{x}|\mathbf{z}_r)) \\ &= \mathcal{L}_{Reg} + \mathcal{L}_{Rec} \end{aligned} \quad (5)$$

with respect to $\boldsymbol{\eta}$ and $\boldsymbol{\gamma}$. Here, $\text{KL}(\cdot, \cdot)$ denotes Kullback-Leibler divergence, and \mathcal{L}_{Reg} and \mathcal{L}_{Rec} represent the regularization and reconstruction errors, respectively. In fact, \mathcal{L}_{Rec} is the cross-entropy that measures how well the model can reconstruct the input data from the latent space, while \mathcal{L}_{Reg} encourages the approximate posterior to be close to the prior distribution over the latent space.

Although the latent space in VAEs is a powerful tool for learning the underlying structure of data, it can face limitations in its capacity to capture the complex features of an input image. When the latent space is not able to fully represent all of the intricate details of an image, the resulting reconstructions can be less accurate and lead to unclear outputs. They tend to distribute probability mass diffusely over the data space, increasing the tendency of VAEs to generate blurry images, as pointed out by Theis et al. (2015). To mitigate the blurriness issue in VAEs, researchers have proposed various modifications such as considering the adversarial loss (Makhzani et al., 2015; Mescheder et al., 2017) in the VAE objective, improving the encoder and decoder network architectures (Yang et al., 2017; Kingma et al., 2016), and using denoising techniques (Im et al., 2017; Creswell and Bharath, 2018). However, the methods mentioned earlier still produce images that exhibit a degree of blurriness.

Meanwhile, the idea of integrating GANs and VAEs was first suggested by Larsen et al. (2016), using the decoder in the VAE as the generator in the GAN. This model, known as the VAE-GAN, provides an alternative approach to addressing the challenges previously mentioned. The paper demonstrates the effectiveness of the VAE-GAN model on several benchmark datasets, showing that it outperforms other unsupervised learning methods in terms of sample quality and diversity. Donahue et al. (2016) and Dumoulin et al. (2016) independently proposed another similar approach in the same manner as in the paper by Larsen et al. (2016). However, their method incorporated a discriminator that not only distinguished between real and fake samples but also jointly compared the real and code samples (encoder output) with the fake and noise (generator input) samples, which sets it apart from the VAE-GAN model.

Another stronger method was proposed by Rosca et al. (2017) called α -GAN. In this approach, the decoder in a VAE was also replaced with the generator of a GAN. Two discriminator networks were then used to optimize the reconstruction and regularization errors of the VAE adversarially. Moreover, a zero-mean Laplace distribution was assigned to the reconstruction data distribution to add an extra term for reconstruction error. This term was considered to provide weights to all parts of the model outputs. Several proxy metrics were employed for evaluating α -GAN models. The findings revealed that the WGPGAN is a robust competitor to the α -GAN and can even surpass it in certain scenarios. Recently, Kwon et al. (2019) proposed a 3D GAN by extending α -GAN for 3D generations. The authors addressed the stability issues of α -GAN and proposed a new hybrid generative model, 3D α -WGPGAN, which employs WGPGAN loss to the α -GAN loss to enhance

training stability. They validated the effectiveness of the 3D α -WGPGAN on some 3D MRI brain datasets, outperforming all previously mentioned models.

2.1.5 3D α -WGPGAN

When $f_{Dec_\gamma}(\mathbf{x}|\mathbf{z}_r)$ in (5) is unknown, \mathcal{L}_{Rec} cannot be employed directly in the training process. One way is assigning a specific distribution to $f_{Dec_\gamma}(\mathbf{x}|\mathbf{z}_r)$, like the Laplace distribution which is a common choice in many VAE-based procedures, and then minimize \mathcal{L}_{Rec} (Ulyanov et al., 2018). However, this procedure can increase subjective constraints in the model (Rosca et al., 2017). An alternative method in approximating $f_{Dec_\gamma}(\mathbf{x}|\mathbf{z}_r)$ is to treat Dec_γ as the generator of a GAN to train the decoder by playing an adversarial game with the GAN discriminator. It guarantees the available training data is fully explored through the training process, thereby preventing mode collapse. Hereinafter, we unify the notation by representing both the VAE decoder and GAN generator as Gen_ω , establishing the connection point between the two models.

The 3D α -WGPGAN incorporates both of the above structures to form a VAE-GAN model (Kwon et al., 2019). The training begins with the VAE, consisting of the Enc_η and Gen_ω components, optimized based on regularization and reconstruction error, as outlined below. This model avoids using Kullback-Leibler divergence in \mathcal{L}_{Reg} to minimize the regularization error which often considers a simple form like a Gaussian for $f_{Enc_\eta}(\mathbf{z}_r|\mathbf{x})$. It defines \mathcal{L}_{Reg} using the Wasserstein distance (40) as

$$\mathcal{L}_{Reg} := W(F_{\mathbf{Z}_r}, F_{Enc_\eta}) = \sup_{\|CDis\|_L \leq 1} E_{F_{\mathbf{Z}_r}}[CDis(\mathbf{Z}_r)] - E_{F_{Enc_\eta}(\mathbf{z}_r|\mathbf{x})}[CDis(\mathbf{Z}_e)], \quad (6)$$

where $\mathbf{Z}_r \sim F_{\mathbf{Z}_r}$ and $\mathbf{Z}_e \sim F_{Enc_\eta}(\mathbf{z}_r|\mathbf{x})$.

Due to the flexibility of neural networks (Arjovsky et al., 2017; Gulrajani et al., 2017), Kwon et al. (2019) considered a family of neural network functions with parameter ξ in a compact domain $\Xi \subset \mathbb{R}^t$, defined in (7), to approximate (6).

$$\mathcal{D}_\xi := \{CDis_\xi \mid E_{F_{\hat{\mathbf{Z}}_r}}[\|\nabla_{\hat{\mathbf{Z}}_r} CDis_\xi(\hat{\mathbf{Z}}_r)\|_2 - 1]^2 = 0, \hat{\mathbf{Z}}_r = (1-u)\mathbf{Z}_r + u\mathbf{Z}_e, 0 \leq u \leq 1, \xi \in \Xi\}. \quad (7)$$

Consequently, \mathcal{L}_{Reg} in (6) can be computed by

$$\mathcal{L}_{Reg} = \max_{\xi \in \Xi} E_{F_{\mathbf{Z}_r}}[CDis_\xi(\mathbf{Z}_r)] - E_{F_{Enc_\eta}(\mathbf{z}_r|\mathbf{x})}[CDis_\xi(\mathbf{Z}_e)].$$

Consideration of the family of neural networks in Eq. (7) constrains $CDis_\xi$ to satisfy the 1-Lipschitz condition (Gulrajani et al., 2017), thereby achieving a meaningful Wasserstein distance metric between the distributions. Kwon et al. (2019) referred to $CDis_\xi$ as a code-discriminator, as it engages in an adversarial game with Enc_η during the minimization of \mathcal{L}_{Reg} to approximate $f_{Enc_\eta}(\mathbf{z}_r|\mathbf{x})$ such that the latent posterior matches to the latent prior $f_{\mathbf{Z}_r}(\mathbf{z}_r)$.

Kwon et al. (2019) assigned a Laplace distribution with mean zero and scale parameter λ to the generator distribution for decoding codes, expressed as $f_{Gen_\omega}(\mathbf{x}|\mathbf{z}_r) \propto e^{-\lambda\|\mathbf{x} - Gen_\omega(\mathbf{z}_e)\|_1}$, where \mathbf{x} represents the original input data observed from the distribution F . Under this formulation, the reconstruction loss \mathcal{L}_{Rec} is expressed as:

$$\mathcal{L}_{Rec} := \lambda E_{F_{Enc_\eta}(\mathbf{z}_r|\mathbf{x})}[\|\mathbf{X} - Gen_\omega(\mathbf{Z}_e)\|_1]. \quad (8)$$

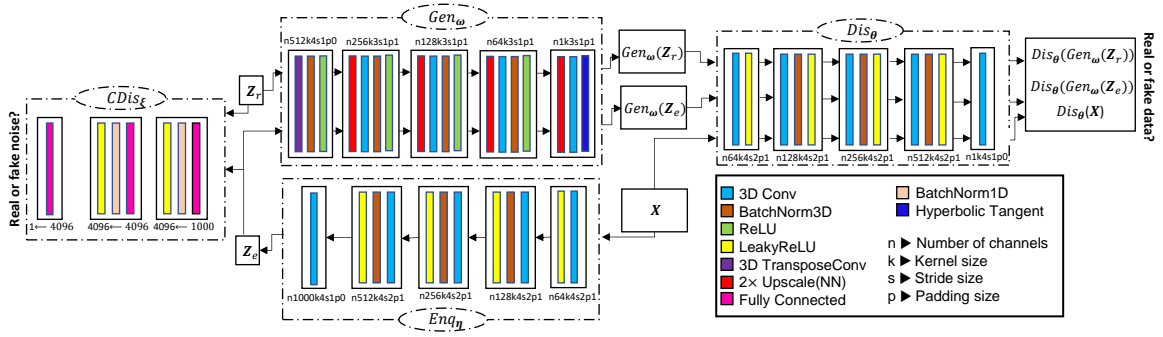


Figure 1: The general architecture of 3D α -WGPGAN comprises three convolutional networks (encoder, generator, and discriminator) and a fully connected-based network (code-discriminator).

The VAE is then trained by minimizing \mathcal{L}_{Reg} and \mathcal{L}_{Rec} , as defined in Eqs. (6) and (8), respectively.

Next, the 3D α -WGPGAN focuses on training the GAN, comprising both the Gen_{ω} and Dis_{θ} components. The GAN is trained by updating the parameters of Gen_{ω} and Dis_{θ} through minimizing the Wasserstein distance between the fake and real samples, formulated as (9), over Ω .

$$W(F, F_{Gen_{\omega}}) = \max_{\theta \in \Theta} E_F[Dis_{\theta}(\mathbf{X})] - E_{F_{Gen_{\omega}}}[Dis_{\theta}(\tilde{\mathbf{X}})]. \quad (9)$$

Here, $\tilde{\mathbf{X}} := (Gen_{\omega}(\mathbf{Z}_r), Gen_{\omega}(\mathbf{Z}_e))$ represents any generated synthetic samples from the generator, and Dis_{θ} belongs to the class of neural network functions \mathcal{D}_{θ} , defined over a compact domain Θ . This class, specified in (10), imposes the 1-Lipschitz constraint on the discriminator (Gulrajani et al., 2017).

$$\mathcal{D}_{\theta} := \{Dis_{\theta} \mid E_{F_{\tilde{\mathbf{X}}}}[\|\nabla_{\tilde{\mathbf{X}}} Dis_{\theta}(\hat{\mathbf{X}})\|_2 - 1]^2 = 0, \hat{\mathbf{X}} = (1 - u)\mathbf{X} + u\tilde{\mathbf{X}}, 0 \leq u \leq 1, \theta \in \Theta\}. \quad (10)$$

The training of the 3D α -WGPGAN is finally achieved by combining the tasks above and minimizing the hybrid loss function:

$$\begin{aligned} \mathcal{L}_{\text{EGen}}(\omega, \eta) = & -E_{F_{Enc_{\eta}}(\mathbf{z}_e|\mathbf{x})}[Dis_{\theta}(Gen_{\omega}(\mathbf{Z}_e))] - E_{F_{\mathbf{Z}_r}}[Dis_{\theta}(Gen_{\omega}(\mathbf{Z}_r))] \\ & + \lambda E_{F_{Enc_{\eta}}(\mathbf{z}_e|\mathbf{x})}[\|\mathbf{X} - Gen_{\omega}(\mathbf{Z}_e)\|_1], \end{aligned} \quad (11)$$

$$\begin{aligned} \mathcal{L}_{\text{Dis}}(\theta) = & E_{F_{Enc_{\eta}}(\mathbf{z}_e|\mathbf{x})}[Dis_{\theta}(Gen_{\omega}(\mathbf{Z}_e))] + E_{F_{\mathbf{Z}_r}}[Dis_{\theta}(Gen_{\omega}(\mathbf{Z}_r))] - 2E_F[Dis_{\theta}(\mathbf{X})] \\ & + \lambda_p E_{F_{\tilde{\mathbf{X}}}}[(\|\nabla_{\tilde{\mathbf{X}}} Dis_{\theta}(\hat{\mathbf{X}})\|_2 - 1)^2], \end{aligned} \quad (12)$$

$$\begin{aligned} \mathcal{L}_{\text{CDis}}(\xi) = & E_{F_{Enc_{\eta}}(\mathbf{z}_e|\mathbf{x})}[CDis_{\xi}(\mathbf{Z}_e)] - E_{F_{\mathbf{Z}_r}}[CDis_{\xi}(\mathbf{Z}_r)] \\ & + \lambda_p E_{F_{\tilde{\mathbf{Z}}_r}}[(\|\nabla_{\tilde{\mathbf{Z}}_r} Dis_{\theta}(\hat{\mathbf{Z}}_r)\|_2 - 1)^2]. \end{aligned}$$

In Equation (12), λ_p is the coefficient of the gradient penalty term $E_{F_{\tilde{\mathbf{X}}}}[(\|\nabla_{\tilde{\mathbf{X}}} Dis_{\theta}(\hat{\mathbf{x}})\|_2 - 1)^2]$. Additionally, the first expectation in Equation (9), which is independent of ω , is

excluded from the gradient descent minimization with respect to ω and thus omitted in Equation (11). All expectations mentioned above are approximated using the empirical distribution in practice.

Kwon et al. (2019) designed the encoder and discriminator networks with five 3D convolutional layers followed by batch normalization (BatchNorm) layers and leaky rectified linear unit (LeakyReLU) activation functions. The generator network includes a transpose convolutional (TransposeConv) layer, four 3D convolutional layers, and a BatchNorm layer with a ReLU activation function in each layer. Typically, BatchNorm and ReLU are applied to ensure network stability. The TransposeConv layer enables the network to “upsample” the input noise vector and generate an output tensor with a larger spatial resolution. The upscale layers are also implemented in the last four layers of the generator network to increase the spatial resolution of the input feature maps. The code-discriminator consists of three fully connected layers followed by BatchNorm and LeakyReLU activation functions. Figure 1 provides a detailed illustration of the architecture of the 3D α -WGPGAN.

2.2 Bayesian Non-parametric Learning

The fundamental concept of BNPL involves placing a prior on the data distribution. We begin by introducing the DP prior, a key element of the BNPL framework.

2.2.1 DIRICHLET PROCESS PRIOR

The DP, introduced by Ferguson (1973), is a widely used prior in BNP methods. It can be seen as a generalization of the Dirichlet distribution, where a random probability measure F is constructed around a fixed probability measure H (the base measure) with variation controlled by a positive real number a (the concentration parameter). Within the context of this statement, H represents the extent of the statistician’s expertise in data distribution, while a denotes the level of intensity of this knowledge.

Definition 1 (Ferguson 1973) *The probability measure F is a DP on a space \mathfrak{X} with a σ -algebra \mathcal{A} of subsets of \mathfrak{X} if, for every measurable partition A_1, \dots, A_K of \mathfrak{X} with $K \geq 2$, the joint distribution of the vector $(F(A_1), \dots, F(A_K))$ has a Dirichlet distribution with parameters $(aH(A_1), \dots, aH(A_K))$. Moreover, it is assumed that $H(A_j) = 0$ implies $F(A_j) = 0$ with probability one.*

One of the most important properties of the DP is its conjugacy property, where the posterior distribution of F given a sample $\mathbf{X}_{1:n}$ drawn from $F \sim DP(a, H)$, denoted by F^{pos} , is also a DP with concentration parameter $a + n$ and base measure $H^* = a(a + n)^{-1}H + n(a + n)^{-1}F_{\mathbf{X}_{1:n}}$, where $F_{\mathbf{X}_{1:n}}$ is the empirical cumulative distribution function of the generated sample $\mathbf{X}_{1:n} := (\mathbf{X}_1, \dots, \mathbf{X}_n)$. This property allows for easy computation of the posterior distribution of F .

Alternative definitions for DP have been proposed, including infinite series representations by Bondesson (1982) and Sethuraman (1994). The method introduced by Sethuraman (1994) is commonly referred to as the stick-breaking representation and is widely used for DP inference. However, Zarepour and Al-Labadi (2012) noted that, unlike the series of Bondesson (1982), the stick-breaking representation lacks normalization terms that convert it into a probability measure. Additionally, simulating from infinite series is only feasible

with a truncation approach for the terms inside the series. Ishwaran and Zarepour (2002) introduced an approximation of DP in the form of a finite series, as shown in (13), which can be easily simulated:

$$F_N^{\text{POS}} = \sum_{i=1}^N J_{i,N}^{\text{POS}} \delta_{\mathbf{X}_i^{\text{POS}}}, \quad (13)$$

where

$$\mathbf{X}_1^{\text{POS}}, \dots, \mathbf{X}_N^{\text{POS}} \stackrel{i.i.d.}{\sim} H^*, \quad (J_{1,N}^{\text{POS}}, \dots, J_{N,N}^{\text{POS}}) \sim \text{Dir}\left(\frac{a+n}{N}, \dots, \frac{a+n}{N}\right),$$

and δ is the Dirac delta measure, which acts as a point mass at each $\mathbf{X}_i^{\text{POS}}$. Specifically, $\delta_{\mathbf{X}_i^{\text{POS}}}(A) = 1$ if $\mathbf{X}_i^{\text{POS}} \in A$ and $\delta_{\mathbf{X}_i^{\text{POS}}}(A) = 0$ otherwise. In this paper, the variables $J_{i,N}^{\text{POS}}$ and $\mathbf{X}_i^{\text{POS}}$ are used to represent the weight and location of the DP, respectively.

Ishwaran and Zarepour (2002) demonstrated that $(F_N^{\text{POS}})_{N \geq 1}$ converges in distribution to F^{POS} , where F_N^{POS} and F^{POS} are random values in the space $M_1(\mathbb{R})$ of probability measures on \mathbb{R} endowed with the topology of weak convergence. To generate $(J_{i,N}^{\text{POS}})_{1 \leq i \leq N}$, one can put $J_{i,N}^{\text{POS}} = \Gamma_{i,N} / \sum_{i=1}^N \Gamma_{i,N}$, where $(\Gamma_{i,N})_{1 \leq i \leq N}$ is a sequence of independent and identically distributed Gamma($(a+n)/N, 1$) random variables that are independent of $(\mathbf{X}_i^{\text{POS}})_{1 \leq i \leq N}$. This form of approximation has been used so far in various applications, including hypothesis testing and GANs, and reflected outstanding results. It also leads to some excellent outcomes in subsequent sections.

The DP approximation given by (13) requires determining the appropriate number of terms to ensure that the truncated series closely resembles the true DP. To determine the appropriate number of terms, we employ a random stopping rule, following the approach introduced by Zarepour and Al-Labadi (2012). This rule adaptively stops the approximation when the contribution of the current term becomes negligible relative to previous terms. Specifically, given a predefined threshold $\varsigma \in (0, 1)$, the stopping point is defined as:

$$N = \inf \left\{ j \mid \frac{\Gamma_{j,j}}{\sum_{i=1}^j \Gamma_{i,j}} < \varsigma \right\}. \quad (14)$$

This method ensures that the series is truncated once additional terms no longer significantly impact the overall approximation, optimizing both computational efficiency and accuracy.

2.2.2 BNPL USING MINIMUM DISTANCE ESTIMATION

Given the placement of a DP prior on the data distribution, Dellaporta et al. (2022) developed a procedure to estimate the parameter of interest using minimum distance estimation, following the BNPL strategy outlined in Lyddon et al. (2018, 2019); Fong et al. (2019). When considering the generator's parameter as the parameter of interest, this strategy defines the generator's parameter as a function of F^{POS} , specifically:

$$\omega^*(F^{\text{POS}}) := \arg \min_{\omega \in \Omega} \Delta(F^{\text{POS}}, F_{\text{Gen}\omega}), \quad (15)$$

where Δ is a statistical distance quantifying the difference between two probability measures.

The key idea is that any posterior distribution over the generator’s parameter space, Ω , can be derived by mapping F^{pos} through the push-forward measure in (15), which is visually represented in Dellaporta et al. (2022, Figure 1). Specifically, Dellaporta et al. (2022) considered Δ as the MMD measure and applied the following DP approximation:

$$F_{n+N}^{\text{pos}} = \sum_{\ell=1}^n \tilde{J}_{\ell,n} \delta_{\mathbf{x}_\ell} + \sum_{t=1}^N J_{t,N} \delta_{\mathbf{v}_t}, \quad (16)$$

where $(\tilde{J}_{1:n,n}, J_{1:N,N}) \sim \text{Dirichlet}(1, \dots, 1, \frac{a}{N}, \dots, \frac{a}{N})$, $(\mathbf{X}_{1:n}) \stackrel{i.i.d.}{\sim} F$, and $(\mathbf{V}_{1:N}) \stackrel{i.i.d.}{\sim} H$.

The BNPL approach effectively addresses model misspecification by adapting a non-parametric prior (Fong et al., 2019; Lyddon et al., 2018, 2019; Lee et al., 2024), supporting a stable learning process, and enhancing generalization across generative tasks. Furthermore, it reduces the model’s sensitivity to outliers and sample variability by incorporating prior regularization, which enhances the stability of out-of-sample performance compared to traditional learning methods that rely solely on the empirical data distribution for computing loss functions (Bariletto and Ho, 2024).

2.2.3 SEMI-BNP MMD GAN

Recently, Fazeli-Asl et al. (2024) proposed training GANs within a BNPL framework using MMD estimation. This method placed a DP prior on the data distribution. Their “Semi-BNP MMD GAN” is a robust BNPL procedure that simulates the posterior distribution in the generator’s parameter space by minimizing the MMD distance between the DP posterior and the generator’s distribution. Although Fazeli-Asl et al. established a generalization error bound and a robustness guarantee for their model under the BNPL approach—enhancing training stability and flexibility—the model still remains prone to mode collapse due to its reliance solely on a GAN framework. This DP approximation offers a notable advantage over the approximation (16) by significantly reducing the number of terms, thus simplifying both the computational and theoretical complexities. Specifically, the method in Fazeli-Asl et al. (2024) scales with $O(N)$, while the approach in Dellaporta et al. (2022) scales with $O(N + n)$.

More precisely, for generated samples $\mathbf{Y}_1, \dots, \mathbf{Y}_m \sim F_{\text{Gen}_\omega}$, $\mathbf{Y}_i := \text{Gen}_\omega(\mathbf{Z}_{r_i})$, and $\mathbf{Z}_{r_i} \sim F_{\mathbf{Z}_r}$, Fazeli-Asl et al. (2024) propose to consider Δ in (15) as the square root of the posterior-based distance defined by:

$$\begin{aligned} \text{MMD}^2(F_N^{\text{pos}}, F_{\text{Gen}_\omega(\mathbf{z}_{r_{1:m}})}) &= \sum_{\ell,t=1}^N J_{\ell,N}^{\text{pos}} J_{t,N}^{\text{pos}} k(\mathbf{X}_\ell^{\text{pos}}, \mathbf{X}_t^{\text{pos}}) - \frac{2}{m} \sum_{\ell=1}^N \sum_{t=1}^m J_{\ell,N}^{\text{pos}} k(\mathbf{X}_\ell^{\text{pos}}, \mathbf{Y}_t) \\ &+ \frac{1}{m^2} \sum_{\ell,t=1}^m k(\mathbf{Y}_\ell, \mathbf{Y}_t). \end{aligned} \quad (17)$$

Fazeli-Asl et al. (2024) considered $k(\cdot, \cdot)$ as a mixture of Gaussian kernels using various bandwidth parameters. For instance, for a set of fixed bandwidth parameters such as $\{\sigma_1, \dots, \sigma_T\}$ and two vectors $\mathbf{X}_\ell^{\text{pos}}$ and \mathbf{Y}_t , $k(\mathbf{X}_\ell^{\text{pos}}, \mathbf{Y}_t) = \sum_{t'=1}^T \exp \frac{-\|\mathbf{X}_\ell^{\text{pos}} - \mathbf{Y}_t\|^2}{2\sigma_{t'}^2}$. Particularly, they used the set of values $\sigma \in \{2, 5, 10, 20, 40, 80\}$, which have been shown to perform

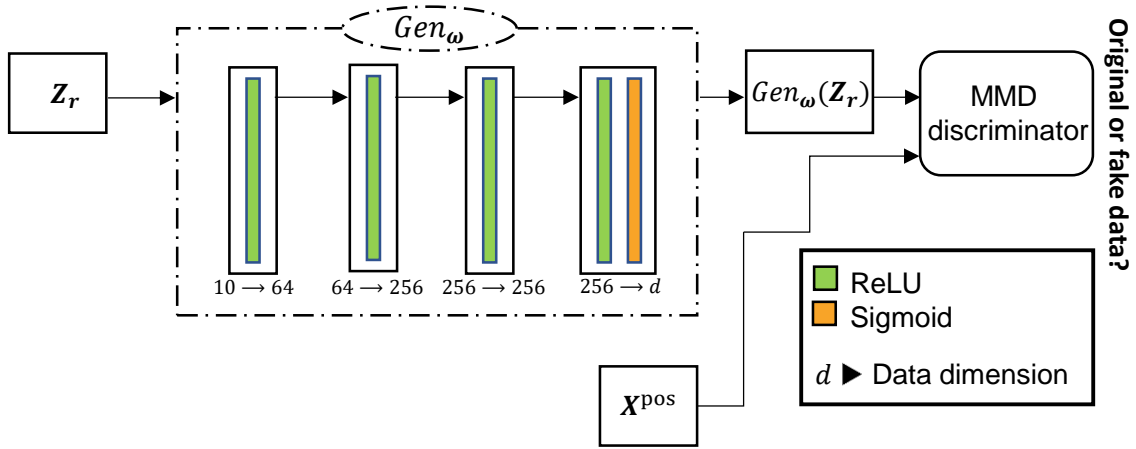


Figure 2: The general architecture of semi-BNP MMD GAN with four ReLU layers and a sigmoid activation function in the final layer.

well in MMD-based training processes (Li et al., 2015). These values have also been considered in our paper to ensure effective performance in MMD-based computations. The generator was implemented using the original architecture proposed by Goodfellow et al. (2014), and the model architecture is illustrated in Figure 2.

3. A Stochastic Representation for Wasserstein Distance

In this section, we present a stochastic procedure for measuring the Wasserstein distance between a fixed probability measure and a random probability measure modeled by a DP prior, specifically tailored for applications in BNPL. For a fixed value of a and a probability measure H , we model the unknown data distribution F as a random probability measure using the following model:

$$\mathbf{X} \sim F, \quad (18)$$

$$F^{\text{pri}} := F \sim DP(a, H), \quad (19)$$

$$F^{\text{pos}} := F | \mathbf{X} \sim DP(a + n, H^*), \quad (20)$$

where $\mathbf{X} = (\mathbf{X}_1, \dots, \mathbf{X}_n)$ represent n samples in \mathbb{R}^d . Let G be any fixed distribution with the ability to simulate samples of any size, and let Dis_θ belong to the 1-Lipschitz family of neural networks \mathcal{D}'_θ , defined over the compact domain $\Theta \subset \mathbb{R}^{t_2}$ in (21).

$$\mathcal{D}'_\theta := \left\{ Dis_\theta \mid \sum_{i=1}^N \frac{[\|\nabla_{\hat{\mathbf{x}}_i^{\text{pos}}} Dis_\theta(\hat{\mathbf{X}}_i^{\text{pos}})\|_2 - 1]^2}{N} = 0, \hat{\mathbf{X}}_i^{\text{pos}} = (1 - u)\mathbf{X}_i^{\text{pos}} + u\mathbf{Y}_i, 0 \leq u \leq 1, \theta \in \Theta \right\}. \quad (21)$$

We propose an approximation for Wasserstein between F^{pos} and G as

$$W(F_N^{\text{pos}}, G_{\mathbf{Y}_{1:N}}) = \max_{\theta \in \Theta} \sum_{i=1}^N \left(J_{i,N}^{\text{pos}} Dis_\theta(\mathbf{X}_i^{\text{pos}}) - \frac{Dis_\theta(\mathbf{Y}_i)}{N} \right), \quad (22)$$

where $(J_{1,N}^{\text{pos}}, \dots, J_{N,N}^{\text{pos}}) \sim \text{Dir}(\frac{a+n}{N}, \dots, \frac{a+n}{N})$, $\mathbf{X}_1^{\text{pos}}, \dots, \mathbf{X}_N^{\text{pos}} \stackrel{i.i.d.}{\sim} H^*$, and $G_{\mathbf{Y}_{1:N}}$ denotes the empirical distribution corresponding to the sample $Y_1, \dots, Y_N \stackrel{i.i.d.}{\sim} G$. We defined (22) using the neural network Dis_{θ} specifically to facilitate its use in the optimization process via gradient descent, as outlined in the following section. The next theorem presents some asymptotic properties of $W(F^{\text{pos}}, G)$ with respect to N, n , and a .

Theorem 2 *Assuming (18)-(20), it follows that for any fixed probability distribution G :*

- i. $W(F_N^{\text{pos}}, G_{\mathbf{Y}_{1:N}}) \xrightarrow{p} W(F, G)$ as $N, n \rightarrow \infty$.
- ii. $W(F_N^{\text{pos}}, G_{\mathbf{Y}_{1:N}}) \xrightarrow{p} W(H, G)$ as $N, a \rightarrow \infty$,

where “ \xrightarrow{p} ” represents convergence in probability and $W(F, G)$ is defined in (9) with $F_{Gen_{\omega}} = G$.

Proof Given that $E_{F^{\text{pos}}}(J_{i,N}^{\text{pos}}) = \frac{1}{N}$ for all $i \in \{1, \dots, N\}$, we can use Chebyshev’s inequality to obtain

$$\Pr \left\{ \left| J_{i,N}^{\text{pos}} - 1/N \right| \geq \epsilon \right\} \leq \frac{\text{Var}_{F^{\text{pos}}}(J_{i,N}^{\text{pos}})}{\epsilon^2}, \quad (23)$$

for any $\epsilon > 0$. Substituting $\text{Var}_{F^{\text{pos}}}(J_{i,N}^{\text{pos}}) = \frac{N-1}{N^2(a+n+1)}$ into (23) and choosing ς in (14) sufficiently small so that $N > n$, yields

$$\Pr \left\{ \left| J_{i,N}^{\text{pos}} - 1/N \right| \geq \epsilon \right\} \leq \frac{N-1}{N^2(a+n+1)\epsilon^2} \leq \frac{1}{n^2}. \quad (24)$$

The convergence of the series $\sum_{n=1}^{\infty} n^{-2}$ implies that $\sum_{n=1}^{\infty} \Pr \left\{ \left| J_{i,N}^{\text{pos}} - 1/N \right| \geq \epsilon \right\} < \infty$. As $n \rightarrow \infty$ in (24), the first Borel-Cantelli lemma implies that $J_{i,N}^{\text{pos}} \xrightarrow{a.s.} 1/N$. Additionally, as n approaches infinity, the Glivenko-Cantelli theorem implies that $F_{\mathbf{X}_{1:n}}$ converges to F and subsequently, H^* converges to F . This convergence indicates that as $n \rightarrow \infty$, the probability of drawing a sample from F approaches 1, implying that $\mathbf{X}_i^{\text{pos}} \rightarrow \mathbf{X}_i$, where \mathbf{X}_i is a random variable distributed according to F , for $i = 1, \dots, N$. By applying the continuous mapping theorem, it follows that $Dis_{\theta}(\mathbf{X}_i^{\text{pos}})$ converges to $Dis_{\theta}(\mathbf{X}_i)$ for any $\theta \in \Theta$, as $n \rightarrow \infty$, and thus, we have

$$\mathcal{I}^{\text{pos}}(\theta) := \sum_{i=1}^N \left(J_{i,N}^{\text{pos}} Dis_{\theta}(\mathbf{X}_i^{\text{pos}}) - \frac{Dis_{\theta}(\mathbf{Y}_i)}{N} \right) \xrightarrow{p} \frac{1}{N} \sum_{i=1}^N (Dis_{\theta}(\mathbf{X}_i) - Dis_{\theta}(\mathbf{Y}_i)). \quad (25)$$

Applying the strong law of large numbers to the right-hand side of Equation (25) yields

$$\mathcal{I}^{\text{pos}}(\theta) \xrightarrow{p} E_F[Dis_{\theta}(\mathbf{X}_1)] - E_G[Dis_{\theta}(\mathbf{Y}_1)],$$

as $N \rightarrow \infty$. Since $\max(\cdot)$ is a continuous function, the proof of (i) is completed by using the continuous mapping theorem. The proof of (ii) is followed by a similar approach. ■

The next corollary demonstrates a crucial property of the $W(F^{\text{pos}}, G)$ metric, which makes it a convenient tool for comparing two models.

Corollary 3 *Assuming the conditions of Theorem 2, then $W(F_N^{\text{pos}}, G_{\mathbf{Y}_{1:N}}) \xrightarrow{p} 0$, if and only if $G = F$, as $N, n \rightarrow \infty$.*

Proof The proof is completed by invoking the equality condition of the Wasserstein distance in part (i) of Theorem 2. \blacksquare

The next Lemma provides a lower bound for the expectation of $W(F_N^{\text{pos}}, G_{\mathbf{Y}_{1:N}})$.

Lemma 4 *Under assumptions of Theorem 2, we have*

$$E[W(F_N^{\text{pos}}, G_{\mathbf{Y}_{1:N}})] \geq W(H^*, G).$$

Proof By virtue of the convexity property of the maximum function, Jensen's inequality implies

$$\begin{aligned} E \left[\max_{\theta \in \Theta} \sum_{i=1}^N \left(J_{i,N}^{\text{pos}} \text{Dis}_{\theta}(\mathbf{X}_i^{\text{pos}}) - \frac{\text{Dis}_{\theta}(\mathbf{Y}_i)}{N} \right) \right] &\geq \max_{\theta \in \Theta} E \left[\sum_{i=1}^N \left(J_{i,N}^{\text{pos}} \text{Dis}_{\theta}(\mathbf{X}_i^{\text{pos}}) - \frac{\text{Dis}_{\theta}(\mathbf{Y}_i)}{N} \right) \right] \\ &= \max_{\theta \in \Theta} \sum_{i=1}^N \frac{1}{N} (E_{H^*}[\text{Dis}_{\theta}(\mathbf{X}_i^{\text{pos}})] - E_G[\text{Dis}_{\theta}(\mathbf{Y}_i)]) \end{aligned} \quad (26)$$

$$= \max_{\theta \in \Theta} E_{H^*}[\text{Dis}_{\theta}(\mathbf{X}_1^{\text{pos}})] - E_G[\text{Dis}_{\theta}(\mathbf{Y}_1)]. \quad (27)$$

Equation (26) is derived from the property of the Dirichlet distribution, while Equation (27) is a result of identical random variables $(\mathbf{X}_i^{\text{pos}})_{1 \leq i \leq N}$ and $(\mathbf{Y}_i)_{1 \leq i \leq N}$. \blacksquare

As noted, the approximation (22) is specifically designed for use within the BNPL procedure, and its application outside this context is unwarranted. Nevertheless, a brief comparison with its frequentist counterpart, based on simple resampling of the empirical data, is informative. While some may argue that a straightforward resampling approach offers a more direct path, this discussion aims to clarify key distinctions and reinforce the rationale behind choosing the DP framework. In approximating the Wasserstein distance using a resampling method, it suffices to substitute $J_{i,N}^{\text{pos}} = 1/N$ and $\mathbf{X}_i^{\text{pos}} = \mathbf{X}'_i$ into (22), where $\mathbf{X}'_1, \dots, \mathbf{X}'_N \stackrel{i.i.d.}{\sim} F_{\mathbf{X}_{1:n}}$ are obtained through simple resampling with replacement. This yields an estimator $W(F_{\mathbf{X}'_{1:N}}, G_{\mathbf{Y}_{1:N}})$ directly based on the data points.

The base measure H in the DP provides distributional regularization by incorporating prior knowledge into the model, reducing sensitivity to sample variability and enhancing stability in the approximation (22). In contrast, resampling may only increase sample size without introducing any prior influence or regularization. As a result, the approximation $W(F_{\mathbf{X}'_{1:N}}, G_{\mathbf{Y}_{1:N}})$ may still exhibit non-smooth behavior, with sharper changes in the approximation, particularly in the presence of high variability or outliers. This effect becomes even more pronounced in mini-batch settings with small samples, leading to greater variability in the Wasserstein approximation across iterations and potential instability in training.

These points highlight the improved out-of-sample performance achieved by BNP estimation procedures compared to the FNP methods, which, by only considering the empirical data distribution, suffer from a lack of out-of-sample performance (Bariletto and Ho, 2024). Additionally, while N is selected in the DP context according to (14), there is no principled basis for choosing the value of N in this resampling approach. These points also hold in the context of the MMD distance and will be demonstrated in Section 5.3.2 with supporting experiments.

4. A Triple Generative Model within BNPL Perspective

In this section, we introduce a triple generative model—comprising a VAE, a CGAN, and a GAN—within the BNPL framework. The BNPL approach is selected for its ability to provide distributional regularization by embedding expert knowledge through the prior distribution, resulting in a robust and stabilized training process with enhanced out-of-sample performance. Furthermore, it effectively addresses model misspecification, enhancing its applicability to challenging generative scenarios.

4.1 Learning Structure

Consider the discriminator Dis_{θ} , which belongs to the 1-Lipschitz family of neural networks \mathcal{D}'_{θ} , and the generator $\{Gen_{\omega}\}_{\omega \in \Omega}$, a family of neural network functions parameterized by ω over a compact domain Ω . The generator maps latent inputs $\{\mathbf{Z}_i\}_{i=1}^N$, where $\mathbf{Z}_i \in \mathbb{R}^p$, into the data space \mathbb{R}^d . Here, \mathbf{Z}_i can be considered any latent variable generated either from the noise distribution or from the encoder distribution. We then employ BNPL by selecting Δ as the distance defined by (28)—a combination of BNP distances given by (22) and (17)—within objective function (15), leading to an implicit approximation of the posterior distribution over Ω .

$$WMMD(F_N^{\text{pos}}, F_{Gen_{\omega}}(\mathbf{z}_{1:N})) := W(F_N^{\text{pos}}, F_{Gen_{\omega}}(\mathbf{z}_{1:N})) + MMD(F_N^{\text{pos}}, F_{Gen_{\omega}}(\mathbf{z}_{1:N})). \quad (28)$$

This choice of Δ not only leverages overall distribution comparison but also results in better feature matching between the generated and original samples by capturing different aspects of the two distributions, thereby improving the stability and quality of the generated samples. The WMMD will contribute to the both components of a VAE-GAN. The complete framework of the triple model—a VAE-GAN calibrated with a CGAN—is then proposed through three main tasks. The GAN serves as the core of the model, which is enhanced by substituting the GAN generator with the VAE decoder. Figure 3 illustrates this connection across all three tasks. This modification plays a crucial role in mitigating mode collapse in the generator and improving its ability to produce sharp images. Our CGAN draws inspiration from the AE+GMMN framework, embedding a GMMN within the latent space of the VAE. This additional step encourages the generator to produce images with less noise.

4.1.1 TASK 1: TRAINING VAE (ENCODER+GENERATOR)

We design our VAE model with an encoder $\{Enc_{\eta}\}_{\eta \in \mathfrak{H}}$, a family of neural network functions parameterized by η over a compact domain \mathfrak{H} , and the generator $\{Gen_{\omega}\}_{\omega \in \Omega}$ —serving as

the connection point between Task 1 and Task 3—by defining its relevant errors as follows. This task is then performed by minimizing these errors to update $\boldsymbol{\eta}$ and $\boldsymbol{\omega}$.

Regularization error: Consider the posterior sample $\mathbf{X}_{1:N}^{\text{pos}}$ generated by (13), along with random noise vectors $\mathbf{Z}_{r_1}, \dots, \mathbf{Z}_{r_N} \stackrel{i.i.d.}{\sim} F_{\mathbf{Z}_r}$ and real codes $\mathbf{Z}_{e_1}, \dots, \mathbf{Z}_{e_N} \stackrel{i.i.d.}{\sim} F_{Enc_{\boldsymbol{\eta}}}$, where \mathbf{Z}_{r_i} and $\mathbf{Z}_{e_i} := Enc_{\boldsymbol{\eta}}(\mathbf{X}_i^{\text{pos}})$ belongs to \mathbb{R}^p . To approximate the variational distribution $F_{Enc_{\boldsymbol{\eta}}}$, we propose minimizing \mathcal{L}_{Reg} over \mathfrak{S} using the MMD distance (39), defined as:

$$\mathcal{L}_{\text{Reg}} := \text{MMD}(F_{\mathbf{Z}_{r_{1:N}}}, F_{\mathbf{Z}_{e_{1:N}}}), \quad (29)$$

where $F_{\mathbf{Z}_{r_{1:N}}}$ and $F_{\mathbf{Z}_{e_{1:N}}}$ are the empirical distributions corresponding to the samples generated from $F_{\mathbf{Z}_r}$ and $F_{Enc_{\boldsymbol{\eta}}}$, respectively. Here, $F_{\mathbf{Z}_r}$ treats as the distribution of the real noise while $F_{Enc_{\boldsymbol{\eta}}}$ treats as the distribution of the fake noise, and thus, minimizing (29) implies that \mathbf{Z}_{e_i} is well-matched to \mathbf{Z}_{r_i} , enabling the generator to thoroughly cover the decoded space. This suggests that the generator has effectively prevented mode collapse (Kwon et al., 2019; Jafari et al., 2023). It is also noted that the distance used in (29) fell outside the scope of the BNP framework, as it involves comparisons between parametric distributions.

In contrast to Kwon et al. (2019), which employed the Wasserstein distance in the code space (a code-discriminator network) to compute \mathcal{L}_{Reg} , leading to significant computational overhead, the computation of \mathcal{L}_{Reg} using (29) is network-free, resulting in reduced computational cost of VAE training.

Reconstruction error: We use the posterior-based WMMD distance (28) to compute \mathcal{L}_{Rec} , defined as:

$$\mathcal{L}_{\text{Rec}} := \text{WMMD}(F_N^{\text{pos}}, F_{Gen_{\boldsymbol{\omega}}(\mathbf{Z}_{e_{1:N}})}). \quad (30)$$

Therefore, minimizing \mathcal{L}_{Rec} over $\boldsymbol{\Omega}$ ensures that the reconstructed samples $Gen_{\boldsymbol{\omega}}(\mathbf{Z}_{e_i})$ closely match the posterior samples $\mathbf{X}_i^{\text{pos}}$ in the data space.

4.1.2 TASK 2: TRAINING CGAN (A GMMN IN THE LATENT SPACE)

To enhance the coverage of the code space, we incorporate a GMMN into the code space of our VAE model. This serves as our CGAN, providing a calibration mechanism for the VAE’s code space. The CGAN includes a generator $\{CGen_{\boldsymbol{\omega}'}\}_{\boldsymbol{\omega}' \in \boldsymbol{\Omega}'}$, a family of neural network functions parameterized by $\boldsymbol{\omega}'$ over a compact domain $\boldsymbol{\Omega}' \subset \mathbb{R}^{t'}$. The code-generator takes random noise samples $\mathbf{Z}'_{r_1}, \dots, \mathbf{Z}'_{r_N} \stackrel{i.i.d.}{\sim} F_{\mathbf{Z}'_r}$ from a sub-latent space \mathbb{R}^q and outputs fake code samples $\tilde{\mathbf{Z}}_{e_1}, \dots, \tilde{\mathbf{Z}}_{e_N} \stackrel{i.i.d.}{\sim} F_{CGen_{\boldsymbol{\omega}'}}$ in the latent space \mathbb{R}^p , where $\tilde{\mathbf{Z}}_{e_i} := CGen_{\boldsymbol{\omega}'}(\mathbf{Z}'_{r_i})$, $q < p$, and $F_{\mathbf{Z}'_r}$ is typically assumed to follow a standard Gaussian distribution.

The objective function (31) is optimized to train $CGen_{\boldsymbol{\omega}'}$, treating $F_{Enc_{\boldsymbol{\eta}}}$ as the distribution of the real code and $F_{CGen_{\boldsymbol{\omega}'}}$ as the distribution of the fake code:

$$\arg \min_{\boldsymbol{\omega}' \in \boldsymbol{\Omega}'} \text{MMD}(F_{\mathbf{Z}_{e_{1:N}}}, F_{\tilde{\mathbf{Z}}_{e_{1:N}}}). \quad (31)$$

The CGAN fills in gaps or unexplored areas of the code space that the VAE may have missed, resulting in better code space coverage and reducing the risk of mode collapse. By

generating more diverse code samples, $CGen_{\omega}$ improves the VAE’s performance. After training the code-generator, the updated weights ω' are frozen, and an additional reconstruction error (32) is incorporated into the VAE training:

$$\mathcal{L}'_{\text{Rec}} := \text{WMMD}(F_N^{\text{pos}}, F_{Gen_{\omega}(\tilde{\mathbf{z}}_{e_{1:N}})}). \quad (32)$$

This encourages Gen_{ω} to produce higher-quality images with reduced noise, particularly in small-sample settings like mini-batches (Li et al., 2015).

4.1.3 TASK 3: TRAINING GAN (GENERATOR+DISCRIMINATOR)

The GAN task is finally achieved by minimizing (33), which updates ω and θ :

$$\mathcal{L}_{\text{GAN}} := \text{WMMD}(F_N^{\text{pos}}, F_{Gen_{\omega}(\mathbf{z}_{r_{1:N}})}). \quad (33)$$

4.1.4 HYBRID LOSS FUNCTION (INTEGRATION OF TASKS 1, 2, AND 3)

The parameters of the triple model are updated using stochastic gradient descent in the following sequence. First, θ is updated by maximizing (30), (32), and (33) over Θ , while keeping ω , η , and ω' fixed to approximate the Wasserstein component of the distance in (28). During this step, posterior MMD-based components of (28) that are independent of θ are ignored. Next, ω' is updated by optimizing (31) with η held constant. Finally, ω and η are updated simultaneously by minimizing (29), (30), (32), and (33) over Ω and \mathfrak{H} , while keeping θ and ω' fixed.

These updates collectively minimize the hybrid loss function (34):

$$\begin{aligned} \mathcal{L}_{\text{Dis}}(\theta) = \sum_{i=1}^N \left(\frac{\text{Dis}_{\theta}(Gen_{\omega}(\mathbf{z}_{r_i})) + \text{Dis}_{\theta}(Gen_{\omega}(\mathbf{z}_{e_i})) + \text{Dis}_{\theta}(Gen_{\omega}(\tilde{\mathbf{z}}_{e_i}))}{N} \right. \\ \left. - 3J_{i,N}^{\text{pos}} \text{Dis}_{\theta}(\mathbf{X}_i^{\text{pos}}) \right) + \lambda_p L_{\text{GP-Dis}}, \end{aligned} \quad (34a)$$

$$\mathcal{L}_{\text{CGen}}(\omega') = \text{MMD}(F_{\mathbf{z}_{e_{1:N}}}, F_{\tilde{\mathbf{z}}_{e_{1:N}}}), \quad (34b)$$

$$\begin{aligned} \mathcal{L}_{\text{EGen}}(\omega, \eta) = - \sum_{i=1}^N \left(\frac{\text{Dis}_{\theta}(Gen_{\omega}(\mathbf{z}_{r_i})) + \text{Dis}_{\theta}(Gen_{\omega}(\mathbf{z}_{e_i})) + \text{Dis}_{\theta}(Gen_{\omega}(\tilde{\mathbf{z}}_{e_i}))}{N} \right) \\ + \text{MMD}(F_N^{\text{pos}}, F_{Gen_{\omega}(\mathbf{z}_{r_{1:N}})}) + \text{MMD}(F_N^{\text{pos}}, F_{Gen_{\omega}(\mathbf{z}_{e_{1:N}})}) \\ + \text{MMD}(F_N^{\text{pos}}, F_{Gen_{\omega}(\tilde{\mathbf{z}}_{e_{1:N}})}) + \text{MMD}(F_{\mathbf{z}_{r_{1:N}}}, F_{\mathbf{z}_{e_{1:N}}}), \end{aligned} \quad (34c)$$

where terms that are independent of ω and η in (30), (32), and (33) are excluded from (34c), as they do not contribute to gradient descent with respect to these parameters. Here, the gradient penalty is given by

$$L_{\text{GP-Dis}} = \frac{1}{N} \sum_{\ell=1}^3 \sum_{i=1}^N \left(\left\| \nabla_{\hat{\mathbf{x}}_{\ell i}^{\text{pos}}} \text{Dis}_{\theta}(\hat{\mathbf{X}}_{\ell i}^{\text{pos}}) \right\|_2 - 1 \right)^2,$$

to constrain Dis_{θ} to satisfy the 1-Lipschitz family (21), where

$$\widehat{\mathbf{X}}_{\ell i}^{\text{pos}} = (1 - u)\mathbf{X}_i^{\text{pos}} + u \times \begin{cases} Gen_{\omega}(\mathbf{Z}_{r_i}) & \text{for } \ell = 1, \\ Gen_{\omega}(\mathbf{Z}_{e_i}) & \text{for } \ell = 2, \\ Gen_{\omega}(\tilde{\mathbf{Z}}_{e_i}) & \text{for } \ell = 3, \end{cases}$$

for $0 \leq u \leq 1$. We set λ_p to 10, a widely recommended value based on Gulrajani et al. (2017), as it performed well across a range of architectures and datasets, from simpler tasks to large-scale models. Algorithm 2 provides a detailed outline of this training procedure.

The distance in (28), forming the central component of Algorithm 2, is interpreted as an estimator of $WMMD(F, F_{Gen_{\omega}})$. The Theorem 5 in Appendix B.1 examines the asymptotic accuracy of $WMMD(F, F_{Gen_{\omega}})$ based on the optimized generator parameter obtained through the BNPL procedure. Furthermore, to understand the impact of outliers on the generator’s performance, we consider Huber’s contamination model (Chérif-Abdellatif and Alquier, 2022), where the data consists of a mixture of a clean distribution and a noise distribution representing outliers. Theorem 6 in Appendix B.2 provides an upper bound on the discrepancy between the clean distribution and the generated distribution, demonstrating that the generator’s performance is affected by the contamination rate, but remains controlled as the rate decreases.

4.2 Selecting the BNP Hyperparameters

The base measure H in the BNP model defined by (18)-(20) reflects the expert’s opinion about the data distribution, instead of assuming a specific distribution for the data population. A Gaussian distribution is a common choice for H , parameterized by the sample mean and sample covariance:

$$\bar{\mathbf{X}} = \frac{1}{n} \sum_{i=1}^n \mathbf{X}_i, \quad S_{\mathbf{X}} = \sum_{i=1}^n (\mathbf{X}_i - \bar{\mathbf{X}})(\mathbf{X}_i - \bar{\mathbf{X}})^T. \quad (35)$$

In our proposed BNPL framework, we use this choice of H in the DP prior (19) to model the data distribution. This prior keeps the model close to the data samples while allowing adaptability to diverse points. It mitigates the influence of outliers, providing a stabilizing regularization effect across the dataset. However, this is a general choice, and one may select a specialized prior based on specific knowledge or requirements.

Furthermore, we choose the optimal value of the concentration parameter a to be its *maximum a posteriori* (MAP) estimate. This is accomplished by maximizing the log-likelihood of F^{pos} with respect to a . Specifically, let \mathbf{A} be a matrix with $K \geq 2$ columns, where each row $\mathbf{A}_{i,\cdot} = (A_{i,1}, \dots, A_{i,K})$ defines a measurable partition of the sample space \mathfrak{X} for $i \in \{1, \dots, n_P\}$, with the rows $\mathbf{A}_{i,\cdot}$ being independent. According to Definition 1 and considering the conjugacy property of DP, given $F^{\text{pos}} \sim DP(a + n, H^*)$, the likelihood for each set of observed probabilities ($F^{\text{pos}}(A_{i,1}) = p_{i,1}, \dots, F^{\text{pos}}(A_{i,K}) = p_{i,K}$) is given by:

$$f(p_{i,1}, \dots, p_{i,K}; a) = \frac{\prod_{k=1}^K \Gamma((a + n)H^*(A_{i,k}))}{\Gamma\left(\sum_{k=1}^K (a + n)H^*(A_{i,k})\right)} \prod_{k=1}^K p_{i,k}^{(a+n)H^*(A_{i,k})-1}. \quad (36)$$

Given the observation matrix $\mathbf{p} = (p_{i,j})_{n_p \times K}$, the log-likelihood for n_p independent sets of observed probabilities \mathbf{p} is given by:

$$\begin{aligned}
LL(a) &= \ln \prod_{i=1}^{n_p} f(p_{i,1}, \dots, p_{i,K}; a) \\
&= \ln \prod_{i=1}^{n_p} \left(\frac{\prod_{k=1}^K \Gamma((a+n)H^*(A_{i,k}))}{\Gamma\left(\sum_{k=1}^K (a+n)H^*(A_{i,k})\right)} \prod_{k=1}^K p_{i,k}^{(a+n)H^*(A_{i,k})-1} \right) \\
&= \sum_{i=1}^{n_p} \left(\sum_{k=1}^K \ln \Gamma((a+n)H^*(A_{i,k})) - \ln \Gamma\left(\sum_{k=1}^K (a+n)H^*(A_{i,k})\right) \right) \\
&\quad + \sum_{i=1}^{n_p} \sum_{k=1}^K ((a+n)H^*(A_{i,k}) - 1) \ln(p_{i,k}), \tag{37}
\end{aligned}$$

To maximize the log-likelihood (37), we calculate the derivative of this log-likelihood with respect to a as

$$\begin{aligned}
\frac{\partial LL(a)}{\partial a} &= \sum_{i=1}^{n_p} \left(\sum_{k=1}^K \psi((a+n)H^*(A_{i,k})) - \psi\left(\sum_{k=1}^K (a+n)H^*(A_{i,k})\right) \right) \\
&\quad + \sum_{i=1}^{n_p} \sum_{k=1}^K H^*(A_{i,k}) \ln(p_{i,k}), \tag{38}
\end{aligned}$$

where $\psi(a) = \partial\Gamma(a)/\partial a$ is the digamma function. we set the derivative in (38) to zero to find the solution. Since there is no closed-form solution for a , we use optimize using L-BFGS-B (Zhu et al., 1997), which supports bound constraints and allows us to specify the range of a , thereby allowing us to select the appropriate level of intensity for our prior knowledge.

To limit the impact of the prior H on the results, we consider an upper bound less than $n/2$ for values of a during the optimization process, as mentioned in Fazeli-Asl et al. (2024). By adhering to this upper bound, we can ensure that the chance of drawing samples from the observed data is at least twice as likely as that of generating samples from H . Furthermore, the K -means algorithm is applied n_p times to define the matrix of partitions $\mathbf{A} = (A_{i,j})_{n_p \times K}$ within the data. Each cluster corresponds to a partition, with sample points assigned to the nearest cluster centroid. The steps outlined above are summarized in Algorithm 1.

4.3 Network Architecture

The architecture of our networks is inspired by the network structure proposed by Kwon et al. (2019). Specifically, we uses the same layers shown in Figure 1 to construct a five 2D convolutional layers network for each of Enc_η , Gen_ω , and Dis_θ , as the main task of this paper is to generate samples in 2-dimensional space. We also follow Kwon et al. (2019) in setting the dimension of the latent space to be $p = 1000$. In the code space,

Algorithm 1: Optimization Process to Approximate Concentration Parameter

Input: Dataset $\mathbf{x}_{1:n}$; $H = N(\bar{\mathbf{x}}, S_{\mathbf{x}})$; partition matrix $\mathbf{A} = (A_{i,j})_{n_P \times K}$; $a_u = \frac{n}{2}$; ϵ .

- 1 Initialize $a \leftarrow a_0$;
- 2 **while** a has not converged **do**
- 3 $F^{\text{pos}} \leftarrow$ Fit a DP posterior $\text{DP}(a + n, H^*)$ to the given dataset \mathbf{x} ;
- 4 $N \leftarrow$ Adjust the number of active terms in the DP approximation using the random stopping rule defined in (14), retaining only those terms with non-negligible weights;
- 5 $F_N^{\text{pos}} \leftarrow$ Approximate F^{pos} using Eq (13);
- 6 $p_{i,j} \leftarrow F_N^{\text{pos}}(A_{i,j})$;
- 7 Compute gradient, $\nabla_a LL(a)$, from Eq. (38), and Hessian of Eq. (37) w.r.t. a , \mathbb{H}^{-1} ;
- 8 $a \leftarrow a - \mathbb{H}^{-1} \nabla_a LL(a)$;
- 9 **if** $a > a_u$ **then**
- 10 | break

Output: a

we use a more sophisticated network architecture for generator $C\text{Gen}_{\omega'}$, which includes three 2D convolutional layers and a fully connected layer, as opposed to the simple network architecture depicted in Figure 2.

To begin, we set the sub-latent input vector size to $q = 100$ in the first layer. Each convolutional layer is accompanied by a batch normalization layer, a ReLU activation function, and a max pooling (MaxPool) layer. The MaxPool layer reduces the spatial size of the feature maps and allows for the extraction of the most significant features of the code samples. Furthermore, it imparts the translation invariance property to the code samples, making Gen_{ω} more robust to variations in the code space. We then use a fully connected layer to transform the feature maps into a code of size $p = 1000$, followed by the addition of a Hyperbolic tangent activation function to the final layer, which squashes the outputs between -1 and 1. To ensure fair comparisons in the code space, we rescale $\mathbf{Z}_{r_{1:N}}$, $\mathbf{Z}_{e_{1:N}}$, and $\tilde{\mathbf{Z}}_{e_{1:N}}$ to be between -1 and 1. The overall architecture of our model is depicted in Figure 3.

5. Experimental Results

In this section, we present the results of our experiments on four datasets to evaluate the performance of our models. We implement our models using the PyTorch library in Python. We set the mini-batch size to 16 and the number of workers to 64. As the Hyperbolic tangent activation function is used on the last layer of the generator, we scaled all datasets to the range of -1 to 1 to ensure compatibility with the generator outputs. For comparison purposes, we evaluated our model against Semi-BNP MMD GAN (Fazeli-Asl et al., 2024) and AE+GMMN (Li et al., 2015)¹. To provide a comprehensive comparison,

1. The relevant codes can be found at <https://github.com/yujiali/gmmn.git>

Algorithm 2: Training Triple-Generative Model via BNPL

Input: Training data $\mathbf{x}_{1:n}$; n_{iter} -iterations; n_{mb} -mini-batch size; learning rates:
 $\alpha_{CGen} = \alpha_{Dis} = \alpha_{Gen} = 2e^{-4}$; penalty $\lambda_p = 10$; threshold $\epsilon = 1e^{-4}$ in (14);
Adam optimizer parameters: ($\epsilon = 1e^{-8}$, $\beta_1 = 0.9$, $\beta_2 = 0.999$).

Output: Optimized parameter of the generator

```

1 for  $t = 1$  to  $n_{\text{iter}}$  do
2   sample  $\mathbf{x}_{1:n_{\text{mb}}} \stackrel{i.i.d.}{\sim} F$ ;
3    $a \leftarrow$  implement Algorithm 1 for batch sample  $\mathbf{x}_{1:n_{\text{mb}}}$ ;
4    $N \leftarrow$  apply  $a$  in (13);
5   Procedure BNPL
6     Posterior sampling from  $\text{DP}(a + n_{\text{mb}}, H^*)$ 
7     sample  $(J_{1,N}^{\text{pos}}, \dots, J_{N,N}^{\text{pos}}) \sim \text{Dir}((a + n_{\text{mb}})/N, \dots, (a + n_{\text{mb}})/N)$ ;
8     sample  $\mathbf{x}_{1:N}^{\text{pos}} \stackrel{i.i.d.}{\sim} H^*$ ;
9      $F_N^{\text{pos}} = \sum_{i=1}^N J_{i,N}^{\text{pos}} \delta_{\mathbf{x}_i^{\text{pos}}}$ ;
10    Updating Discriminator
11    sample noises  $\mathbf{z}_{r_{1:N}} \stackrel{i.i.d.}{\sim} F_{\mathbf{z}_r}$  and  $\mathbf{z}'_{r_{1:N}} \stackrel{i.i.d.}{\sim} F_{\mathbf{z}'_r}$ ;
12     $\tilde{\mathbf{z}}_{e_{1:N}} = CGen_{\omega'}(\mathbf{z}'_{r_{1:N}})$ ,  $\mathbf{z}_{e_{1:N}} = Enc_{\eta}(\mathbf{x}_{1:N}^{\text{pos}})$ ;
13     $(\tilde{\mathbf{x}}_{1:N}^{\text{pos}}, \tilde{\mathbf{x}}_{N+1:2N}^{\text{pos}}, \tilde{\mathbf{x}}_{2N+1:3N}^{\text{pos}}) = (Gen_{\omega}(\mathbf{z}_{r_{1:N}}), Gen_{\omega}(\mathbf{z}_{e_{1:N}}), Gen_{\omega}(\tilde{\mathbf{z}}_{e_{1:N}}))$ ;
14    computing gradient penalty
15     $u \sim U(0, 1)$ ,  $L_{\text{GP-Dis}} \leftarrow 0$ ;
16    for  $\ell = 1$  to 3 do
17       $\hat{\mathbf{x}}_{\ell,1:N}^{\text{pos}} = (1 - u)\mathbf{x}_{1:N}^{\text{pos}} + u\tilde{\mathbf{x}}_{((\ell-1)N+1):\ell N}^{\text{pos}}$ ;
18       $L_{\text{GP-Dis}} \leftarrow N^{-1} \sum_{i=1}^N (\|\nabla_{\hat{\mathbf{x}}_{\ell,i}^{\text{pos}}} Dis_{\theta}(\hat{\mathbf{x}}_{\ell,i}^{\text{pos}})\|_2 - 1)^2 + L_{\text{GP-Dis}}$ ;
19     $\mathcal{L}_{\text{GAN}} \leftarrow \text{WMMD}(F_N^{\text{pos}}, F_{\tilde{\mathbf{x}}_{1:N}^{\text{pos}}})$ ;
20     $\mathcal{L}_{\text{Rec}} \leftarrow \text{WMMD}(F_N^{\text{pos}}, F_{\tilde{\mathbf{x}}_{N+1:2N}^{\text{pos}}})$ ;
21     $\mathcal{L}'_{\text{Rec}} \leftarrow \text{WMMD}(F_N^{\text{pos}}, F_{\tilde{\mathbf{x}}_{2N+1:3N}^{\text{pos}}})$ ;
22     $\mathcal{L} \leftarrow -(\mathcal{L}_{\text{Rec}} + \mathcal{L}'_{\text{Rec}} + \mathcal{L}_{\text{GAN}}) + \lambda_p L_{\text{GP-Dis}}$ ;
23     $\nabla_{\theta} \mathcal{L}_{\text{Dis}}(\theta) \leftarrow \nabla_{\theta} \mathcal{L}$ ;
24     $\theta \leftarrow \text{Adam}(\nabla_{\theta} \mathcal{L}_{\text{Dis}}(\theta), \theta, \epsilon, \beta_1, \beta_2)$ ;
25    Updating Code-Generator
26    repeat lines (11)–(12);
27     $\mathcal{L}_{\text{CGen}}(\omega') \leftarrow \text{MMD}(F_{\mathbf{z}_{e_{1:N}}}, F_{\tilde{\mathbf{z}}_{e_{1:N}}})$ ;
28     $\omega' \leftarrow \text{Adam}(\nabla_{\omega'} \mathcal{L}_{\text{CGen}}(\omega'), \omega', \epsilon, \beta_1, \beta_2)$ ;
29    Updating Encoder & Generator/Decoder
30    repeat lines (11)–(13) and then lines (19)–(21) sequentially;
31     $\mathcal{L}_{\text{Reg}} \leftarrow \text{MMD}(F_{\mathbf{z}_{r_{1:N}}}, F_{\mathbf{z}_{e_{1:N}}})$ ;
32     $\mathcal{L} \leftarrow \mathcal{L}_{\text{Reg}} + \mathcal{L}_{\text{Rec}} + \mathcal{L}'_{\text{Rec}} + \mathcal{L}_{\text{GAN}}$ ;
33     $\nabla_{(\omega, \eta)} \mathcal{L}_{\text{EGen}}(\omega, \eta) \leftarrow \nabla_{(\omega, \eta)} \mathcal{L}$ ;
34     $(\omega, \eta) \leftarrow \text{Adam}(\nabla_{(\omega, \eta)} \mathcal{L}_{\text{EGen}}(\omega, \eta), (\omega, \eta), \epsilon, \beta_1, \beta_2)$ ;

```

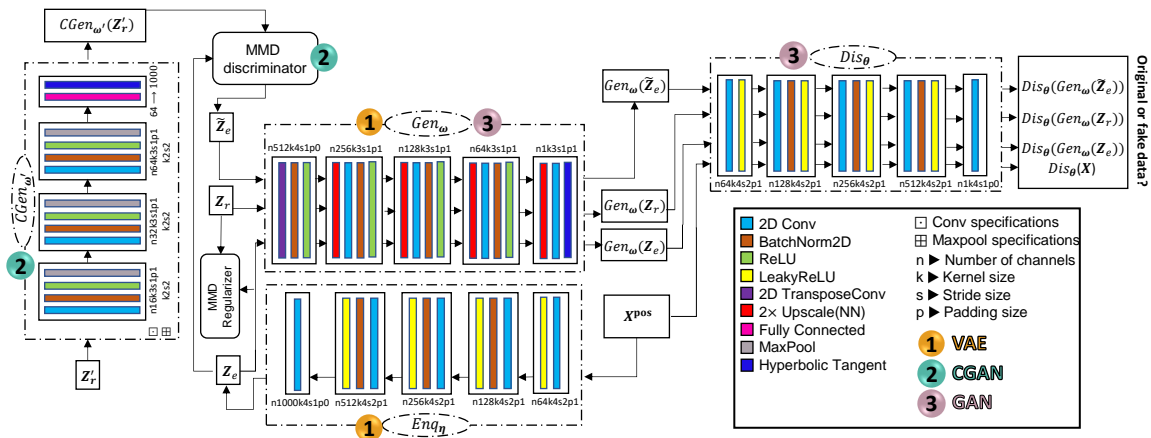


Figure 3: The general architecture of the proposed triple model consists of four convolutional networks for the encoder, generator, code-generator, and discriminator. The partial models—VAE, CGAN, and GAN—are labeled as 1, 2, and 3, respectively.

we also attempted to modify the 3D α -WPGAN (Kwon et al., 2019)² settings to the 2D dimension case and included its relevant results. Table 1 presents the shared and distinct attributes of these models in relation to our proposed model.

Table 1: Comparative analysis of generative models: Highlighting shared and distinct attributes

Model	Wasserstein	MMD	CGAN	VAE	GAN	AE
Ours	✓	✓	✓	✓	✓	✗
Semi-BNP MMD (Fazeli-Asl et al., 2024)	✗	✓	✗	✗	✓	✗
AE+GMMN (Li et al., 2015)	✗	✓	✓	✗	✗	✓
α -WPGAN (Kwon et al., 2019)	✓	✗	✗	✓	✓	✗

5.1 Labeled Datasets

To evaluate model performance, we analyzed two handwritten datasets comprising of numbers (MNIST) and letters (EMNIST). MNIST consists of 60,000 handwritten digits, including 10 numbers from 0 to 9 (labels), each with 784 (28×28) dimensions. This dataset was divided into 50,000 training and 10,000 testing images, and we use the training set to train the network (LeCun, 1998). EMNIST is freely available online³ and is sourced from Cohen et al. (2017). It contains 372,450 samples of the 26 letters A-Z (labels). Each letter is represented in a 28×28 dimension. We allocate 85% of the samples to the training dataset, and the rest to the testing dataset.

2. The basic code for 3D generation are available at <https://github.com/cyclomon/3dbraingen>

3. <https://www.kaggle.com/datasets/sachinpatel21/az-handwritten-alphabets-in-csv-format>

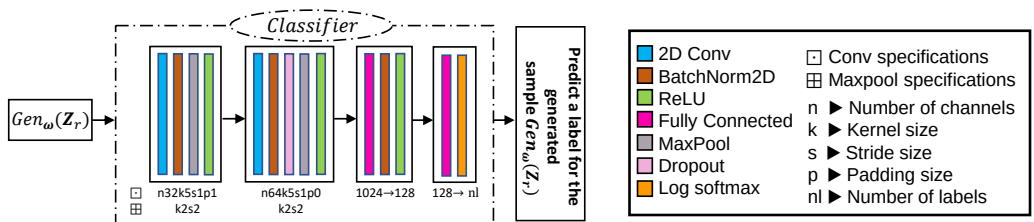


Figure 4: The classifier network architecture for predicting the handwritten dataset’s labels. The output of the fully connected layer is passed through a log softmax function to convert the raw output into a probability distribution over the classes.

5.1.1 EVALUATING MODE COLLAPSE

To examine the capability of the model in covering all modes or preventing the mode collapse, we train a convolutional network to predict the label of each generated sample. The structure of this network is provided in Figure 4. If the generator has effectively tackled the issue of the mode collapse, we anticipate having a similar relative frequency for labels in both training and generated datasets, indicating successful training. Plots (a) and (b) in Figure 6 represent the relative frequency of labels in handwritten numbers and letters datasets, respectively.

To train the classifier, we use the cross-entropy loss function and update the network’s weights with the Adam optimizer over 60 epochs. We assess the classifier’s efficacy by presenting the mean of the loss function across all mini-batch testing samples and the percentage of correct classification (accuracy rate) in Figure 5. The figure showcases the classifier’s exceptional accuracy in classifying the dataset.

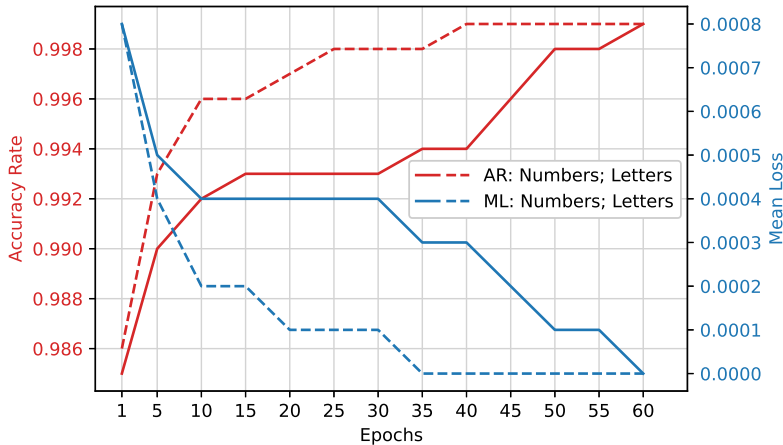


Figure 5: The convolutional classifier’s mean loss (ML) and accuracy rate (AR) with a learning rate of 0.0002 across all mini-batch testing samples of numbers (solid line) and letters (dashed line) datasets.

The relative frequency plots of predicted labels are depicted in Figure 6, parts (c)-(j), for 1000 generated numbers (left-hand side) and letters (right-hand side) using various

generative models. The ratios of the numbers in the training dataset are expected to be consistent, as indicated by plot (a). Examining the plot of generated samples reveals that each model has a distinct bias towards certain digits. Specifically, our model tends to produce digit 6 at a frequency 4.64% higher than that in the training dataset (14.50% – 9.86%), while the semi-BNP MMD GAN exhibits a similar bias towards digit 3 at a 4.18% higher frequency than the training dataset.

Nevertheless, these differences are relatively minor compared to AE+GMMN and α -WGPGAN, which demonstrate a significant tendency to memorize some modes and overlook certain digits, such as 4 and 8. Similar results can be observed from the relative frequency plots of predicted labels for the letters dataset. Plot (j) in Figure 6 clearly shows the failure of α -WGPGAN to maintain the balance of the relative frequency of the data and generate the letter “M”. In contrast, plot (d) indicates that our proposed model successfully preserves the proportion of modes in the generated samples and avoids mode collapse.

5.1.2 ASSESSING PATTERNS AND EVALUATING MODEL QUALITY

We employed the principal component analysis (PCA) to illustrate the latent structure among data points in a two-dimensional space. Parts (a) and (b) in Figure 7 represent the PCA plots for numbers and letters, respectively. Each axis in the plots represents a principal component, with the relevant real dataset used as a reference. It is important to note that PCA provides a necessary condition to verify the similarity pattern between real and fake data distribution (Hotelling, 1933). The dissimilarity between PCA plots for real and generated samples indicates that they do not follow the same distribution. However, two similar PCA plots do not necessarily guarantee a similar distribution for real and generated samples. Here, the results presented in Figure 7 demonstrate that all models follow the pattern of the relevant real datasets except for the α -WGPGAN in the letters dataset. It indicates a different shape and orientation than the structure of the real dataset.

For a more comprehensive analysis, we adopt a mini-batch strategy suggested by Fazeli-Asl et al. (2024) to compute the MMD score, as given by Equation (39), between the generated and real samples. We present the discrepancy scores in density and box plots, along with violin plots in Figure 7, parts (c) and (d). Overall, the MMD scores of all four models suggest some level of convergence around zero. However, the results of the proposed model and the semi-BNP model are comparable, with both models showing better convergence than the other two models. Specifically, part (d) shows our proposed model demonstrates even better convergence than the semi-BNP model, highlighting an improvement of the semi-BNP MMD model by extending it to the VAE+WMMMD model.

5.1.3 VISUALISATION

To better demonstrate the visual capabilities of our proposed model in generating samples, we have displayed 60 samples generated from the model and have compared them to the samples generated by other models, as depicted in Figure 8. While the semi-BNP MMD model displays a range of generated characters in parts (e) and (f) of Figure 8, the images contain some noise that detracts from their quality. On the other hand, the results of AE+GMMN, displayed in parts (g) and (h), reveal blurry outputs that fall short of our desired standards. In contrast, the outputs of our model and α -WGPGAN exhibit higher-

resolution samples without any noise. However, it appears that the generated samples of the α -WGPGAN model contain slightly more ambiguous images compared to ours, suggesting that our model converges faster than α -WGPGAN.

5.2 Unlabeled Datasets

The performance of a GAN can vary depending on the characteristics of the training dataset, including its complexity, diversity, quality, and size. Thus, it is crucial to assess the model’s effectiveness on more intricate datasets. For a comprehensive evaluation of the model’s performance, facial and medical images are the two most important datasets to consider. In this regard, we use the following two main data sources and resize all images within them to 64×64 pixels to train all models.

5.2.1 BRAIN MRI DATASET

The brain MRI images present a complex medical dataset that poses a significant challenge for researchers. These images can be easily accessed online⁴, with both training and testing sets available, comprising a total of 7,023 images of human brain MRI. The dataset includes glioma, meningioma, no tumor, and pituitary tumors (Nickparvar, 2021). The training set is composed of 5,712 images of varying sizes, each with extra margins. To ensure consistency and reduce noise in the training data, a pre-processing code⁵ is used to remove margins before feeding them into the networks for training.

Part (a) of Figure 9 illustrates the PCA plots of the generated samples for all models, highlighting that the dispersion and direction of samples generated by α -WGPGAN model differ the most from the real dataset compared to the other models. Meanwhile, part (c) of Figure 9 shows almost identical convergence of MMD scores around zero for the compared models. However, Figure 10 portrays noisy and blurry outputs generated by the semi-BNP and AE+GMMN models, whereas our model and the α -WGPGAN produce clear outputs.

5.2.2 CELEBFACES ATTRIBUTES DATASET

The CelebFaces attributes dataset (CelebA), collected by Liu et al. (2015), includes 202,599 images of celebrities that are publicly available online⁶. The dataset features people in various poses, with different backgrounds, hairstyles and colors, skin tones, and wearing or not wearing glasses and hats, providing a rich resource for evaluating the performance of data augmentation models. While part (b) of Figure 9 shows a slight variation in the direction of the generated sample pattern, part (d) of the same figure highlights a significant gap between the convergence of MMD scores of our proposed approach and α -WGPGAN compared to semi-BNP MMD and AE+GMMN around zero. Our proposed model yields even lower MMD scores than α -WGPGAN.

On the other hand, despite the limited number of samples shown in Figure 11, the generated images by our proposed model exhibit a remarkable diversity that encompasses a range of hair colors and styles, skin tones, and accessories such as glasses and hats. This variety suggests that our results are comparable to those produced by α -WGPGAN.

4. <https://www.kaggle.com/dsv/2645886>

5. <https://github.com/masoudnick/Brain-Tumor-MRI-Classification/blob/main/Preprocessing.py>

6. <http://mmlab.ie.cuhk.edu.hk/projects/CelebA.html>

However, it is worth noting that the images generated by the AE+GMMN model not only suffer from blurriness but also appear to be heavily biased toward female faces, indicating a potential issue with mode collapse in this type of dataset. While the samples generated by the semi-BNP MMD model displayed better results than the AE+GMMN, there is still a level of noise present, indicating that more iterations are needed to ensure model convergence.

5.3 Comparative Analysis of the BNP Model

Although the proposed model outperformed well-known baselines, further investigation is required to understand the individual contributions of each component within the triple model. Additionally, there is interest in exploring how the BNPL framework impacts training stability. These concerns are addressed in the following sections.

5.3.1 TRIPLE MODEL VS. PARTIAL MODELS

We evaluate 1000 samples generated by the triple model against two partial models within the BNPL framework: VAE-GAN (dual model) and GAN (single model). Figure 12 presents box plots of MMD scores for each model across all datasets considered in this study. The results demonstrate the significant advantage of the triple model over the dual model, as well as the dual model over the single model. Progressing from the single model to the triple model results in reduced MMD scores, indicating improved performance and greater diversity in the generated samples.

To further illustrate the differences among the triple, dual, and single models, we particularly provide relative frequency plots of predicted labels for generated handwritten digits as determined by the trained classifier shown in Figure 4. Figure 13a demonstrates that the triple model more effectively preserves the frequency percentage of labels compared to the other two models, highlighting its superior performance. Figure 13b depicts the absolute differences between the frequency percentages of real and generated samples across all labels. The results show that minimizing these absolute differences across labels is most effectively achieved by the triple model, whereas the single GAN model performs the worst.

With particular attention, although the dual model shows improved diversity compared to the single GAN, as evidenced in Figures 13a and 13b, it still produces unclear samples (highlighted by the red square within the green frame in Figure 13c). These unclear samples confuse the classifier in predicting digit labels, ultimately affecting the diversity of the generated samples. This highlights the limitation of the dual model, further emphasizing the advantage of the triple model in generating both diverse and clear samples.

5.3.2 BNPL COMPARED TO THE FNP COUNTERPART USING RESAMPLING TECHNIQUE

The training performance of BNPL is compared to its exact FNP counterpart, which employs a resampling technique, as described in the final paragraph of Section 3. During each iteration of the training process with a mini-batch sample $\mathbf{X}_{1:n_{mb}}$, instead of applying the BNP approximation (28) for training the generator, a simple resampling technique with replacement is used. This involves drawing samples $\mathbf{X}'_1, \dots, \mathbf{X}'_{2n_{mb}} \stackrel{i.i.d.}{\sim} F_{\mathbf{X}_{1:n_{mb}}}$ to compute

the exact FNP counterpart $WMMD(F_{\mathbf{X}'_{1:2n_{mb}}}, F_{Gen_{\omega}(\mathbf{Z}_{1:2n_{mb}})})$, where \mathbf{Z}_i is a latent variable sampled from either the noise distribution or the encoder distribution.

It is worth emphasizing that N in BNP approximation (28) is a random variable, as defined by (14) within the DP context. Therefore, it is not meaningful to use N as the resampling size in the FNP counterpart. Instead, a resampling size of $2n_{mb}$ was chosen for these experiments, as there is no specific rule for determining this parameter.

Figure 14 presents the WMMD values over different iterations for both strategies across all datasets included in this study. The results demonstrate notably reduced variation in learning rates for BNPL compared to its FNP counterpart, along with improved convergence. These findings suggest more stabilized training under the BNPL framework.

6. Conclusion

We have proposed a powerful triple generative model that has produced realistic samples within the BNPL framework. We have extended the semi-BNP MMD GAN, introduced by Fazeli-Asl et al. (2024), by incorporating both Wasserstein and MMD measures into the GAN loss function along with a VAE and an CGAN to enhance its ability to produce diverse outputs. Different types of datasets have been used to examine the performance of the proposed model, indicating that it is a competitive model. Our model has also been compared to several generative models, such as α -WGPGAN, and has outperformed them in terms of mitigating mode collapse and producing noise-free images.

To improve the efficiency and effectiveness of communication between the generator and discriminator networks, we plan to employ multiplex networks in our model. Multiplex networks can tackle the problem of data sparsity in GANs by incorporating multiple types of interactions and relationships between nodes. This allows the model to learn from a larger and more diverse set of data, improving its ability to generate realistic samples. For future work, we are considering extending our proposed idea to include 3D medical datasets for detecting anomalies like Down’s syndrome in fetuses. This development could prevent the birth of defective babies. We hope that a more powerful generative model can help solve important issues in medical imaging.

References

- M. Arjovsky and L. Bottou. Towards principled methods for training generative adversarial networks. *CoRR*, abs/1701.04862, 2017. URL <http://arxiv.org/abs/1701.04862>.
- M. Arjovsky, S. Chintala, and L. Bottou. Wasserstein generative adversarial networks. In *International Conference on Machine Learning*, pages 214–223. PMLR, 2017.
- N. Bariletto and N. Ho. Bayesian nonparametrics meets data-driven distributionally robust optimization. In *The Thirty-eighth Annual Conference on Neural Information Processing Systems*, 2024. URL <https://openreview.net/forum?id=8CguPoe3TP>.
- Y. Bengio, P. Lamblin, D. Popovici, and H. Larochelle. Greedy layer-wise training of deep networks. *Advances in Neural Information Processing Systems*, 19, 2006.

- L. Bondesson. On simulation from infinitely divisible distributions. *Advances in Applied Probability*, 14(4):855–869, 1982.
- B.-E. Chérief-Abdellatif and P. Alquier. Finite sample properties of parametric MMD estimation: Robustness to misspecification and dependence. *Bernoulli*, 28(1):181–213, 2022.
- G. Cohen, S. Afshar, J. Tapson, and A. Van Schaik. EMNIST: Extending MNIST to handwritten letters. In *2017 International Joint Conference on Neural Networks*, pages 2921–2926. IEEE, 2017.
- A. Creswell and A. A. Bharath. Denoising adversarial autoencoders. *IEEE Transactions on Neural Networks and Learning Systems*, 30(4):968–984, 2018.
- C. Dellaporta, J. Knoblauch, T. Damoulas, and F.-X. Briol. Robust Bayesian inference for simulator-based models via the MMD posterior bootstrap. In *International Conference on Artificial Intelligence and Statistics*, pages 943–970. PMLR, 2022.
- J. Donahue, P. Krähenbühl, and T. Darrell. Adversarial feature learning. *arXiv preprint arXiv:1605.09782*, 2016.
- V. Dumoulin, I. Belghazi, B. Poole, O. Mastropietro, A. Lamb, M. Arjovsky, and A. Courville. Adversarially learned inference. *arXiv preprint arXiv:1606.00704*, 2016.
- G. K. Dziugaite, D. M. Roy, and Z. Ghahramani. Training generative neural networks via maximum mean discrepancy optimization. In *Proceedings of the Thirty-First Conference on Uncertainty in Artificial Intelligence*, pages 258–267, 2015.
- F. Fazeli-Asl, M. M. Zhang, and L. Lin. A semi-bayesian nonparametric estimator of the maximum mean discrepancy measure: Applications in goodness-of-fit testing and generative adversarial networks. *Transactions on Machine Learning Research*, 2024. ISSN 2835-8856. URL <https://openreview.net/forum?id=1UnlHS1FYT>.
- T. S. Ferguson. A Bayesian analysis of some nonparametric problems. *The Annals of Statistics*, 1(2):209–230, 1973.
- E. Fong, S. P. Lyddon, and C. C. Holmes. Scalable nonparametric sampling from multimodal posteriors with the posterior bootstrap. In *International Conference on Machine Learning*, pages 1952–1962. PMLR, 2019.
- I. Goodfellow, J. Pouget-Abadie, M. Mirza, B. Xu, D. Warde-Farley, S. Ozair, A. Courville, and Y. Bengio. Generative adversarial nets. *Advances in Neural Information Processing Systems*, 27:2672–2680, 2014.
- A. Gretton, K. M. Borgwardt, M. J. Rasch, B. Schölkopf, and A. Smola. A kernel two-sample test. *The Journal of Machine Learning Research*, 13(1):723–773, 2012.
- I. Gulrajani, F. Ahmed, M. Arjovsky, V. Dumoulin, and A. C. Courville. Improved training of Wasserstein GANs. *Advances in Neural Information Processing Systems*, 30, 2017.

- H. Hotelling. Analysis of a complex of statistical variables into principal components. *Journal of educational psychology*, 24(6):417, 1933.
- D. Im, S. Ahn, R. Memisevic, and Y. Bengio. Denoising criterion for variational auto-encoding framework. In *Proceedings of the AAAI Conference on Artificial Intelligence*, volume 31, 2017.
- H. Ishwaran and M. Zarepour. Exact and approximate sum representations for the Dirichlet process. *Canadian Journal of Statistics*, 30(2):269–283, 2002.
- S. M. Jafari, M. Cevik, and A. Basar. Improved α -GAN architecture for generating 3D connected volumes with an application to radiosurgery treatment planning. *Applied Intelligence*, pages 1–27, 2023.
- D. P. Kingma and M. Welling. Auto-encoding variational Bayes. *arXiv preprint arXiv:1312.6114*, 2013.
- D. P. Kingma, T. Salimans, R. Jozefowicz, X. Chen, I. Sutskever, and M. Welling. Improved variational inference with inverse autoregressive flow. *Advances in neural information processing systems*, 29, 2016.
- N. Kodali, J. Abernethy, J. Hays, and Z. Kira. On convergence and stability of GANs. *arXiv preprint arXiv:1705.07215*, 2017.
- G. Kwon, C. Han, and D.-S. Kim. Generation of 3D brain MRI using auto-encoding generative adversarial networks. In *Medical Image Computing and Computer Assisted Intervention—MICCAI 2019: 22nd International Conference, Shenzhen, China, October 13–17, 2019, Proceedings, Part III 22*, pages 118–126. Springer, 2019.
- A. B. L. Larsen, S. K. Sønderby, H. Larochelle, and O. Winther. Autoencoding beyond pixels using a learned similarity metric. In *International conference on machine learning*, pages 1558–1566. PMLR, 2016.
- Y. LeCun. The MNIST database of handwritten digits. 1998. URL <http://yann.lecun.com/exdb/mnist/>.
- H. Lee, G. Nam, E. Fong, and J. Lee. Enhancing transfer learning with flexible nonparametric posterior sampling. *arXiv preprint arXiv:2403.07282*, 2024.
- Y. Li, K. Swersky, and R. Zemel. Generative moment matching networks. In *International Conference on Machine Learning*, pages 1718–1727. PMLR, 2015.
- Z. Liu, P. Luo, X. Wang, and X. Tang. Deep learning face attributes in the wild. In *Proceedings of International Conference on Computer Vision (ICCV)*, December 2015.
- S. P. Lyddon, S. G. Walker, and C. C. Holmes. Nonparametric learning from Bayesian models with randomized objective functions. *Advances in Neural Information Processing Systems*, 31, 2018.
- S. P. Lyddon, C. C. Holmes, and S. G. Walker. General Bayesian updating and the loss-likelihood bootstrap. *Biometrika*, 106(2):465–478, 2019.

- Q. Ma, M. Dong, C. Xia, X. He, R. Chen, M. Ren, and M. Song. A multivariate normal distribution data generative model in small-sample-based fault diagnosis: Taking traction circuit breaker as an example. *IEEE Transactions on Intelligent Transportation Systems*, 2024.
- A. Makhzani, J. Shlens, N. Jaitly, I. Goodfellow, and B. Frey. Adversarial autoencoders. *arXiv preprint arXiv:1511.05644*, 2015.
- L. Mescheder, S. Nowozin, and A. Geiger. Adversarial variational Bayes: Unifying variational autoencoders and generative adversarial networks. In *International Conference on Machine Learning*, pages 2391–2400. PMLR, 2017.
- A. Müller. Integral probability metrics and their generating classes of functions. *Advances in Applied Probability*, 29(2):429–443, 1997.
- M. Nickparvar. Brain tumor MRI dataset, 2021. <https://www.kaggle.com/dsv/2645886>.
- M. Rosca, B. Lakshminarayanan, D. Warde-Farley, and S. Mohamed. Variational approaches for auto-encoding generative adversarial networks. *arXiv preprint arXiv:1706.04987*, 2017.
- T. Salimans, I. Goodfellow, W. Zaremba, V. Cheung, A. Radford, and X. Chen. Improved techniques for training GANs. *Advances in Neural Information Processing Systems*, 29, 2016.
- J. Sethuraman. A constructive definition of Dirichlet priors. *Statistica sinica*, pages 639–650, 1994.
- L. Theis, A. van den Oord, and M. Bethge. A note on the evaluation of generative models. *arXiv preprint arXiv:1511.01844*, 2015.
- D. Ulyanov, A. Vedaldi, and V. Lempitsky. It takes (only) two: Adversarial generator-encoder networks. In *Proceedings of the AAAI Conference on Artificial Intelligence*, volume 32, 2018.
- C. Villani. Optimal transport, old and new. *Grundlehren der mathematischen Wissenschaften*, 3, 2008.
- Z. Yang, Z. Hu, R. Salakhutdinov, and T. Berg-Kirkpatrick. Improved variational autoencoders for text modeling using dilated convolutions. In *International conference on machine learning*, pages 3881–3890. PMLR, 2017.
- M. Zarepour and L. Al-Labadi. On a rapid simulation of the Dirichlet process. *Statistics & Probability Letters*, 82(5):916–924, 2012.
- C. Zhu, R. H. Byrd, P. Lu, and J. Nocedal. Algorithm 778: L-BFGS-B: Fortran subroutines for large-scale bound-constrained optimization. *ACM Transactions on Mathematical Software*, 23(4):550–560, 1997.

Appendix

A. Integral Probability Metrics

Given a data space \mathfrak{X} , let \mathbf{X} and \mathbf{Y} be random variables that follow distributions F_1 and F_2 , respectively, where $F_1, F_2 \in \mathcal{P}(\mathfrak{X})$, the set of all probability measures over the Borel σ -algebra on \mathfrak{X} . To measure the discrepancy between F_1 and F_2 , an integral probability metric (IPM) is used, defined as:

$$\text{IPM}(F_1, F_2) = \sup_{S \in \mathcal{S}} |E_{F_1}[S(\mathbf{X})] - E_{F_2}[S(\mathbf{Y})]|,$$

where \mathcal{S} is a class of functions chosen to emphasize significant differences between F_1 and F_2 . The specific choice of \mathcal{S} determines the particular distance used (Müller, 1997).

A.1 Maximum Mean Discrepancy Distance

A prominent example of an IPM is the maximum mean discrepancy (MMD), which arises when \mathcal{S} is taken as the unit ball in a reproducing kernel Hilbert space (RKHS) \mathcal{H}_k defined by a positive-definite kernel $k : \mathfrak{X} \times \mathfrak{X} \rightarrow \mathbb{R}$ (Gretton et al., 2012). Specifically:

$$\mathcal{S}_H = \{H \in \mathcal{H}_k \mid \|H\|_{\mathcal{H}_k} \leq 1\},$$

where $\|\cdot\|_{\mathcal{H}_k}$ denotes the RKHS norm. The positive-definite nature of the kernel k allows functions $H \in \mathcal{H}_k$ to be represented for any $\mathbf{X} \in \mathfrak{X}$ as:

$$H(\mathbf{X}) = \langle H, k(\mathbf{X}, \cdot) \rangle_{\mathcal{H}_k},$$

where $\langle \cdot, \cdot \rangle_{\mathcal{H}_k}$ is the inner product in \mathcal{H}_k . The *kernel mean embedding* of a distribution F , as described by Gretton et al. (2012), is defined as:

$$\mu_F(\cdot) = E_F[k(\mathbf{X}, \cdot)] \in \mathcal{H}_k.$$

The MMD between F_1 and F_2 is then expressed by:

$$\text{MMD}(F_1, F_2) = \sup_{H \in \mathcal{S}_H} (E_{F_1}[H(\mathbf{X})] - E_{F_2}[H(\mathbf{Y})]) = \|\mu_{F_1} - \mu_{F_2}\|_{\mathcal{H}_k},$$

which can be expanded as:

$$\text{MMD}^2(F_1, F_2) = E_{F_1}[k(\mathbf{X}, \mathbf{X}')] - 2E_{F_1, F_2}[k(\mathbf{X}, \mathbf{Y})] + E_{F_2}[k(\mathbf{Y}, \mathbf{Y}')],$$

where $\mathbf{X}, \mathbf{X}' \stackrel{i.i.d.}{\sim} F_1$ and $\mathbf{Y}, \mathbf{Y}' \stackrel{i.i.d.}{\sim} F_2$, assuming $E_F[\sqrt{k(\mathbf{X}, \mathbf{X})}] < \infty$ for all $F \in \mathcal{P}(\mathfrak{X})$.

In real scenarios, when the distributions F_1 and F_2 are unknown, the MMD is typically approximated using samples $\mathbf{X}_{1:n} := (\mathbf{X}_1, \dots, \mathbf{X}_n) \sim F_1$ and $\mathbf{Y}_{1:m} := (\mathbf{Y}_1, \dots, \mathbf{Y}_m) \sim F_2$. The V-statistic estimator using empirical distributions $F_{\mathbf{X}_{1:n}} := \frac{1}{n} \sum_{i=1}^n \delta_{\mathbf{X}_i}$ and $F_{\mathbf{Y}_{1:m}} := \frac{1}{m} \sum_{i=1}^m \delta_{\mathbf{Y}_i}$ is represented by:

$$\text{MMD}^2(F_{\mathbf{X}_{1:n}}, F_{\mathbf{Y}_{1:m}}) = \frac{1}{n^2} \sum_{i=1}^n \sum_{j=1}^n k(\mathbf{X}_i, \mathbf{X}_j) - \frac{2}{nm} \sum_{i=1}^n \sum_{j=1}^m k(\mathbf{X}_i, \mathbf{Y}_j) + \frac{1}{m^2} \sum_{i=1}^m \sum_{j=1}^m k(\mathbf{Y}_i, \mathbf{Y}_j). \quad (39)$$

An alternative approach involves using an unbiased U-statistic estimator. The MMD satisfies the condition $\text{MMD}^2(F_1, F_2) = 0$ if and only if $F_1 = F_2$ (equality condition), assuming that \mathcal{H}_k is a universal reproducing kernel Hilbert space (RKHS) over a compact metric space \mathfrak{X} with a continuous kernel function k (Gretton et al., 2012, Theorem 5).

A.2 Wasserstein Distance

Given the compact metric space \mathfrak{X} , the Wasserstein distance, defined using the Kantorovich-Rubinstein duality (Villani, 2008), is expressed as:

$$W(F_1, F_2) = \sup_{D \in \mathcal{S}_D} (E_{F_1}[D(\mathbf{X})] - E_{F_2}[D(\mathbf{Y})]), \quad (40)$$

where

$$\mathcal{S}_D = \{D : \mathfrak{X} \rightarrow \mathbb{R}^l \mid \|D\|_L \leq 1\}$$

represents the set of all 1-Lipschitz functions, with $\|\cdot\|_L$ denoting the Lipschitz norm. The 1-Lipschitz condition implies that for any $\mathbf{X}_1, \mathbf{X}_2 \in \mathfrak{X}$,

$$\|D(\mathbf{X}_1) - D(\mathbf{X}_2)\|_2 \leq \|\mathbf{X}_1 - \mathbf{X}_2\|_2,$$

where $\|\cdot\|_2$ represents the Euclidean norm.

This representation of the Wasserstein distance highlights its role as an IPM. It satisfies the equality condition $W(F_1, F_2) = 0$ if and only if $F_1 = F_2$. Moreover, when D is differentiable, the 1-Lipschitz condition can be equivalently expressed as $\|\nabla_{\mathbf{X}} D(\mathbf{X})\|_2 \leq 1$ for all $\mathbf{X} \in \mathfrak{X}$, where $\nabla_{\mathbf{X}} D(\mathbf{X})$ denotes the gradient of D with respect to \mathbf{X} . For the optimal differentiable 1-Lipschitz function $D^{(\text{opt})}$, it can be shown that $\|\nabla_{\widehat{\mathbf{X}}} D^{(\text{opt})}(\widehat{\mathbf{X}})\|_2 = 1$, almost everywhere, where $\widehat{\mathbf{X}} = (1 - u)\mathbf{X} + u\mathbf{Y}$ for $0 \leq u \leq 1$ (Gulrajani et al., 2017, Corollary 1). Consequently, it may simplify the optimization process to focus on the subclass of 1-Lipschitz functions that maintain a gradient norm of 1 at $\widehat{\mathbf{X}}$.

In practical applications, the distance in (40) is estimated using the empirical distributions, yielding

$$W(F_{\mathbf{X}_{1:n}}, F_{\mathbf{Y}_{1:n}}) = \sup_{D \in \mathcal{S}_D} \left(\sum_{i=1}^n \frac{D(\mathbf{X}_i)}{n} - \sum_{i=1}^m \frac{D(\mathbf{Y}_i)}{m} \right).$$

B. Additional Theoretical Results

B.1 Assessing the Accuracy of BNPL Estimation

Theorem 5 *Assuming (18)-(20), consider the generator $\{Gen_{\omega}\}_{\omega \in \Omega}$, and let ω_{BNPL}^* denote the optimized parameter value obtained through Algorithm 2. Let ω_{True} be the parameter value satisfying*

$$WMMD(F, F_{Gen_{\omega_{True}}}) = 0, \quad (41)$$

in the well-specified case. Let $k(\cdot, \cdot)$ be a continuous kernel function with a feature space corresponding to a universal RKHS, defined on a compact metric space X , and assume

$|k(t, t')| < K$ for all $t, t' \in \mathbb{R}^d$. Furthermore, suppose there exists a finite constant $M > 0$ such that

$$\max(W(F, F_{\mathbf{X}_{1:n}}), W(F, H^*)) < M, \quad (42)$$

for any $n \in \mathbb{N}$. Then, as $n, N \rightarrow \infty$,

$$\limsup E \left[\text{WMMD} \left(F, F_{\text{Gen}_{\omega^*_{\text{BNPL}}}} \right) \right] = 0.$$

Proof The triangular inequality implies:

$$\text{WMMD}(F, F_{\text{Gen}_{\omega^*_{\text{BNPL}}}}) \leq \text{WMMD}(F, F_N^{\text{pos}}) + \text{WMMD}(F_N^{\text{pos}}, F_{\text{Gen}_{\omega^*_{\text{BNPL}}}}) = I_1.$$

Regarding definition of ω^*_{BNPL} , for any $\omega \in \Omega$, we have:

$$\begin{aligned} I_1 &\leq \text{WMMD}(F, F_N^{\text{pos}}) + \text{WMMD}(F_N^{\text{pos}}, F_{\text{Gen}_{\omega}}) \\ &\leq \text{WMMD}(F, F_N^{\text{pos}}) + \text{WMMD}(F_N^{\text{pos}}, F) + \text{WMMD}(F, F_{\text{Gen}_{\omega}}) \quad (\text{Triangle inequality}) \\ &\leq 2 [\text{WMMD}(F, F_{\mathbf{X}_{1:n}}) + \text{WMMD}(F_{\mathbf{X}_{1:n}}, F_N^{\text{pos}})] + \text{WMMD}(F, F_{\text{Gen}_{\omega}}) \quad (\text{Triangle inequality}) \\ &\leq 2 [\text{WMMD}(F, F_{\mathbf{X}_{1:n}}) + \text{WMMD}(F_{\mathbf{X}_{1:n}}, H^*) + \text{WMMD}(H^*, F_N^{\text{pos}})] + \text{WMMD}(F, F_{\text{Gen}_{\omega}}) \\ &\quad (\text{Triangle inequality}) \end{aligned}$$

Therefore,

$$\begin{aligned} \text{WMMD}(F, F_{\text{Gen}_{\omega^*_{\text{BNPL}}}}) &\leq 2 [\text{WMMD}(F, F_{\mathbf{X}_{1:n}}) + \text{WMMD}(F_{\mathbf{X}_{1:n}}, H^*) + \text{WMMD}(F_N^{\text{pos}}, H^*)] \\ &\quad + \min_{\omega \in \Omega} \text{WMMD}(F, F_{\text{Gen}_{\omega}}) \\ &= 2 [\text{WMMD}(F, F_{\mathbf{X}_{1:n}}) + \text{WMMD}(F_{\mathbf{X}_{1:n}}, H^*) + \text{WMMD}(F_N^{\text{pos}}, H^*)] \\ &\quad (\text{Applying assumption (41)}) \\ &= 2[\text{W}(F, F_{\mathbf{X}_{1:n}}) + \text{W}(F_{\mathbf{X}_{1:n}}, H^*) + \text{W}(F_N^{\text{pos}}, H^*) \\ &\quad + \text{MMD}(F, F_{\mathbf{X}_{1:n}}) + \text{MMD}(F_{\mathbf{X}_{1:n}}, H^*) + \text{MMD}(F_N^{\text{pos}}, H^*)] \\ &= 2[2\text{W}(F, F_{\mathbf{X}_{1:n}}) + \text{W}(F, H^*) + \text{W}(F_N^{\text{pos}}, H^*) \\ &\quad + \text{MMD}(F, F_{\mathbf{X}_{1:n}}) + \text{MMD}(F_{\mathbf{X}_{1:n}}, H^*) + \text{MMD}(F_N^{\text{pos}}, H^*)] \\ &\quad (\text{Triangle inequality}). \end{aligned} \quad (43)$$

Taking the expectation of both sides of (43), we get:

$$\begin{aligned} E \left[\text{WMMD} \left(F, F_{\text{Gen}_{\omega^*_{\text{BNPL}}}} \right) \right] &\leq 2\{2E[\text{W}(F, F_{\mathbf{X}_{1:n}})] + E[\text{W}(F, H^*)] + E[\text{W}(F_N^{\text{pos}}, H^*)] \\ &\quad + E[\text{MMD}(F, F_{\mathbf{X}_{1:n}})] + E[\text{MMD}(F_{\mathbf{X}_{1:n}}, H^*)] \\ &\quad + E[\text{MMD}(F_N^{\text{pos}}, H^*)]\} \end{aligned} \quad (44)$$

Using Chérif-Abdellatif and Alquier (2022, Lemma 7.1), Dellaporta et al. (2022, Lemma 8), and the proof of Fazeli-Asl et al. (2024, Lemma 4), it follows that:

$$E[\text{MMD}(F, F_{\mathbf{X}_{1:n}})] + E[\text{MMD}(F_{\mathbf{X}_{1:n}}, H^*)] + E[\text{MMD}(F_N^{\text{pos}}, H^*)] \leq \frac{2K}{\sqrt{n}} + \frac{4aK}{a+n} + 2\sqrt{\frac{(a+n+N)K}{(a+n+1)N}}. \quad (45)$$

Given the optimized value $\theta^* \in \Theta$ for approximating $W(F_N^{\text{pos}}, H^*)$, consider two independent copies of the random variables, $\mathbf{X}_{1:N}^{\text{pos}}$ and $\mathbf{X}_{1:N}^{\text{pos}'}$, where $\mathbf{X}_{1:N}^{\text{pos}}, \mathbf{X}_{1:N}^{\text{pos}'}$ $\overset{i.i.d.}{\sim} H^*$. Then, it follows that

$$\begin{aligned} E[W(F_N^{\text{pos}}, H^*)] &= E \sum_{i=1}^N \left(J_{i,N}^{\text{pos}} \text{Dis}_{\theta^*}(\mathbf{X}_i^{\text{pos}}) - \frac{\text{Dis}_{\theta^*}(\mathbf{X}_i^{\text{pos}'})}{N} \right) \\ &= \sum_{i=1}^N \left(\frac{1}{N} E_{H^*}(\text{Dis}_{\theta^*}(\mathbf{X}_i^{\text{pos}})) - \frac{E_{H^*}(\text{Dis}_{\theta^*}(\mathbf{X}_i^{\text{pos}'})}{N} \right) \quad (\text{Dirichlet variables}) \\ &= E_{H^*}(\text{Dis}_{\theta^*}(\mathbf{X}_1^{\text{pos}})) - E_{H^*}(\text{Dis}_{\theta^*}(\mathbf{X}_1^{\text{pos}'})) \quad (\text{Identical random variables}) \\ &= 0 \quad (\text{Identical random variables}). \end{aligned} \quad (46)$$

Applying (45) and (46) to (44), and then taking the limsup of both sides of (44) as n and N go to infinity, we obtain:

$$\begin{aligned} 0 \leq \limsup E \left[\text{WMMD} \left(F, F_{\text{Gen}_{\omega^*_{\text{BNPL}}}} \right) \right] &\leq 4 \limsup E(W(F, F_{\mathbf{X}_{1:n}})) + 2 \limsup E(W(F, H^*)) \\ &\leq 4E(\limsup W(F, F_{\mathbf{X}_{1:n}})) + 2E(\limsup W(F, H^*)), \end{aligned} \quad (47)$$

where the last inequality follows from considering assumption (42) and then applying the reverse Fatou's lemma.

Finally, considering the Glivenko-Cantelli theorem, which ensures that $F_{\mathbf{X}_{1:n}}$ converges to F and, consequently, that H^* converges to F , we then use Arjovsky et al. (2017, Theorem 2) on the right-hand side of (47), completing the proof. \blacksquare

B.2 Assessing BNPL Estimation in the Presence of Outliers

Theorem 6 Consider Huber's contamination model (Chérif-Abdellatif and Alquier, 2022), defined as $F = (1 - \varepsilon)F_0 + \varepsilon Q$, where F_0 represents the clean distribution, Q denotes the noise distribution accounting for outliers, and $\varepsilon \in (0, \frac{1}{2})$ is the contamination rate. $\mathbf{X}_i \sim F_0$ if $\zeta_i = 0$; otherwise, $X_i \sim Q$, where $\zeta_1, \dots, \zeta_n \overset{i.i.d.}{\sim} \text{Bernoulli}(\varepsilon)$. Assuming $W(F_0, Q) = c$, $c < \infty$, then, under assumption of Theorem 5, as $n, N \rightarrow \infty$,

$$\limsup E \left[\text{WMMD} \left(F_0, F_{\text{Gen}_{\omega^*_{\text{BNPL}}}} \right) \right] \leq (2 + c)\varepsilon.$$

Proof Regarding Chérif-Abdellatif and Alquier (2022, Lemma 3.3), for $\omega_{\text{BNPL}}^* \in \Omega$,

$$|\text{MMD}(F, F_{\text{Gen}\omega_{\text{BNPL}}^*}) - \text{MMD}(F_0, F_{\text{Gen}\omega_{\text{BNPL}}^*})| \leq 2\varepsilon.$$

It implies that

$$\begin{aligned} \text{WMMD}\left(F_0, F_{\text{Gen}\omega_{\text{BNPL}}^*}\right) &\leq \text{W}\left(F_0, F_{\text{Gen}\omega_{\text{BNPL}}^*}\right) + \text{MMD}\left(F, F_{\text{Gen}\omega_{\text{BNPL}}^*}\right) + 2\varepsilon \\ &\leq \text{W}(F_0, F) + \text{WMMD}\left(F, F_{\text{Gen}\omega_{\text{BNPL}}^*}\right) + 2\varepsilon \quad (\text{Triangle inequality}). \end{aligned} \quad (48)$$

On the other hand, since $F = (1 - \varepsilon)F_0 + \varepsilon Q$, for any $\theta \in \Theta$, we can derive the following:

$$\begin{aligned} E_{F_0}[\text{Dis}_\theta(\mathbf{X})] - E_F[\text{Dis}_\theta(\mathbf{Y})] &= \int_{\mathfrak{X}} \text{Dis}_\theta(\mathbf{x}) dF_0(\mathbf{x}) - \int_{\mathfrak{X}} \text{Dis}_\theta(\mathbf{y}) dF(\mathbf{y}) \\ &= \int_{\mathfrak{X}} \text{Dis}_\theta(\mathbf{x}) dF_0(\mathbf{x}) - (1 - \varepsilon) \int_{\mathfrak{X}} \text{Dis}_\theta(\mathbf{y}) dF_0(\mathbf{y}) - \varepsilon \int_{\mathfrak{X}} \text{Dis}_\theta(\mathbf{y}) dQ(\mathbf{y}) \\ &= \varepsilon \left(\int_{\mathfrak{X}} \text{Dis}_\theta(\mathbf{y}) dF_0(\mathbf{y}) - \int_{\mathfrak{X}} \text{Dis}_\theta(\mathbf{y}) dQ(\mathbf{y}) \right) \\ &= \varepsilon (E_{F_0}[\text{Dis}_\theta(\mathbf{Y})] - E_Q[\text{Dis}_\theta(\mathbf{Y})]). \end{aligned} \quad (49)$$

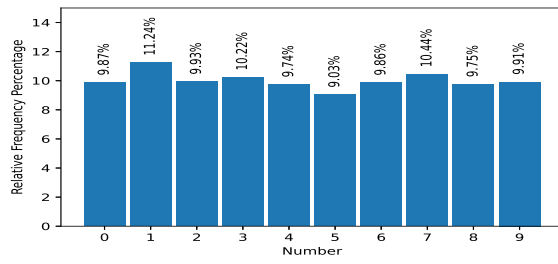
Taking the supremum of both sides of (49) over Θ , we obtain:

$$\text{W}(F_0, F) = \varepsilon \text{W}(F_0, Q) = \varepsilon c. \quad (50)$$

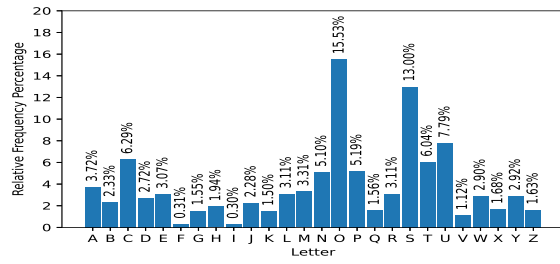
Now, considering (50) in (48) and taking the expectation, we get:

$$E\left(\text{WMMD}\left(F_0, F_{\text{Gen}\omega_{\text{BNPL}}^*}\right)\right) \leq (2 + c)\varepsilon + E\left(\text{WMMD}\left(F, F_{\text{Gen}\omega_{\text{BNPL}}^*}\right)\right). \quad (51)$$

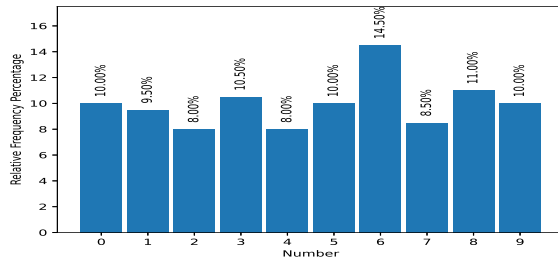
Finally, taking the lim sup of both sides of (51) and applying Theorem 5 completes the proof. ■



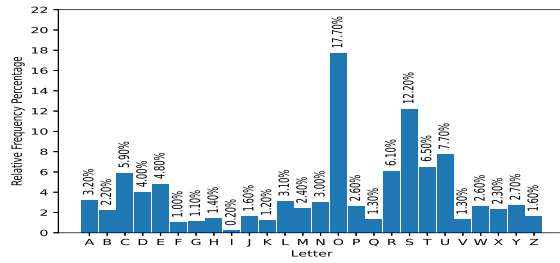
(a) Numbers: Training dataset



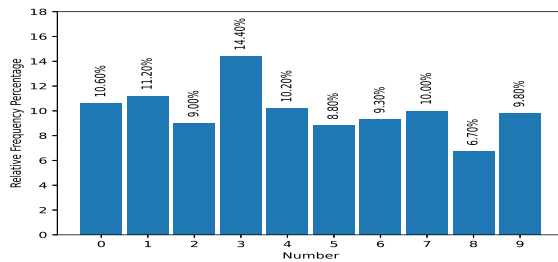
(b) Letters: Training dataset



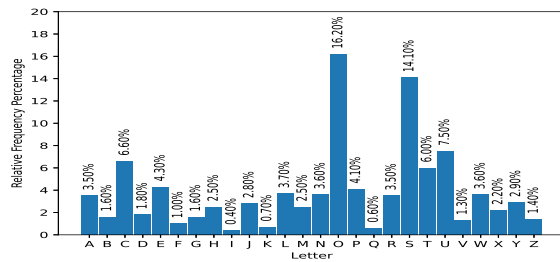
(c) Ours



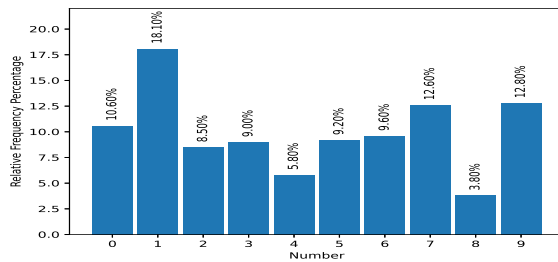
(d) Ours



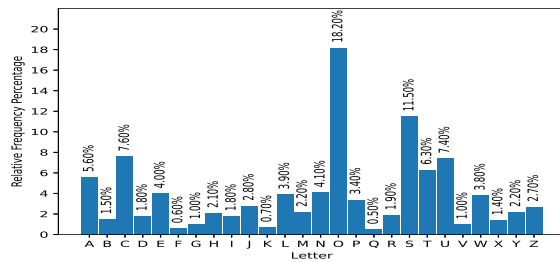
(e) Semi-BNP MMD



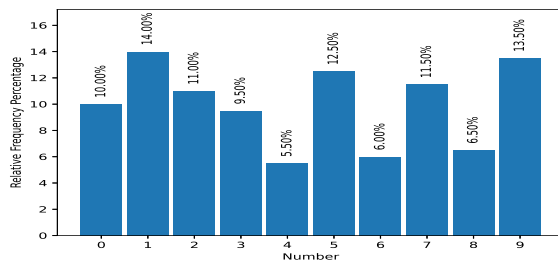
(f) Semi-BNP MMD



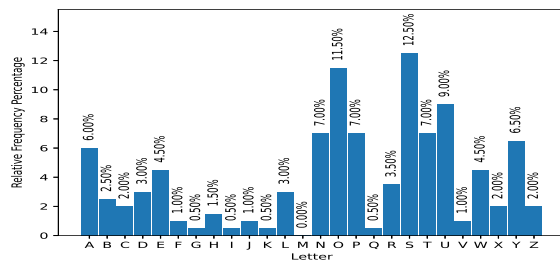
(g) AE+GMMN



(h) AE+GMMN



(i) α -WPGAN



(j) α -WPGAN

Figure 6: The frequency percentage of true and predicted labels for handwritten datasets.

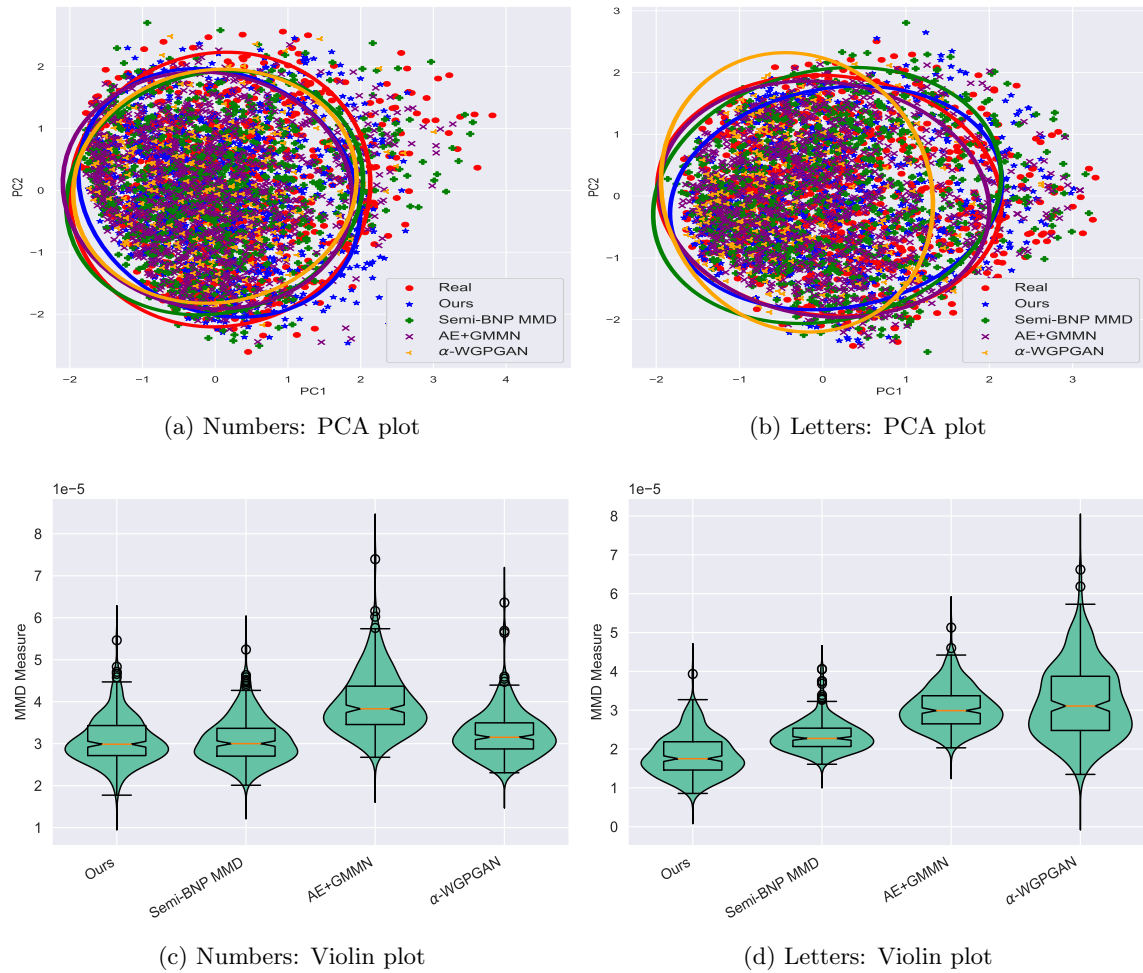


Figure 7: Top: PCA plots of 1000 generated samples versus real samples with fitted ellipse curves for handwritten datasets, indicating the spread of the samples in the corresponding directions. Bottom: Violin plots of MMD scores including density and box plots.

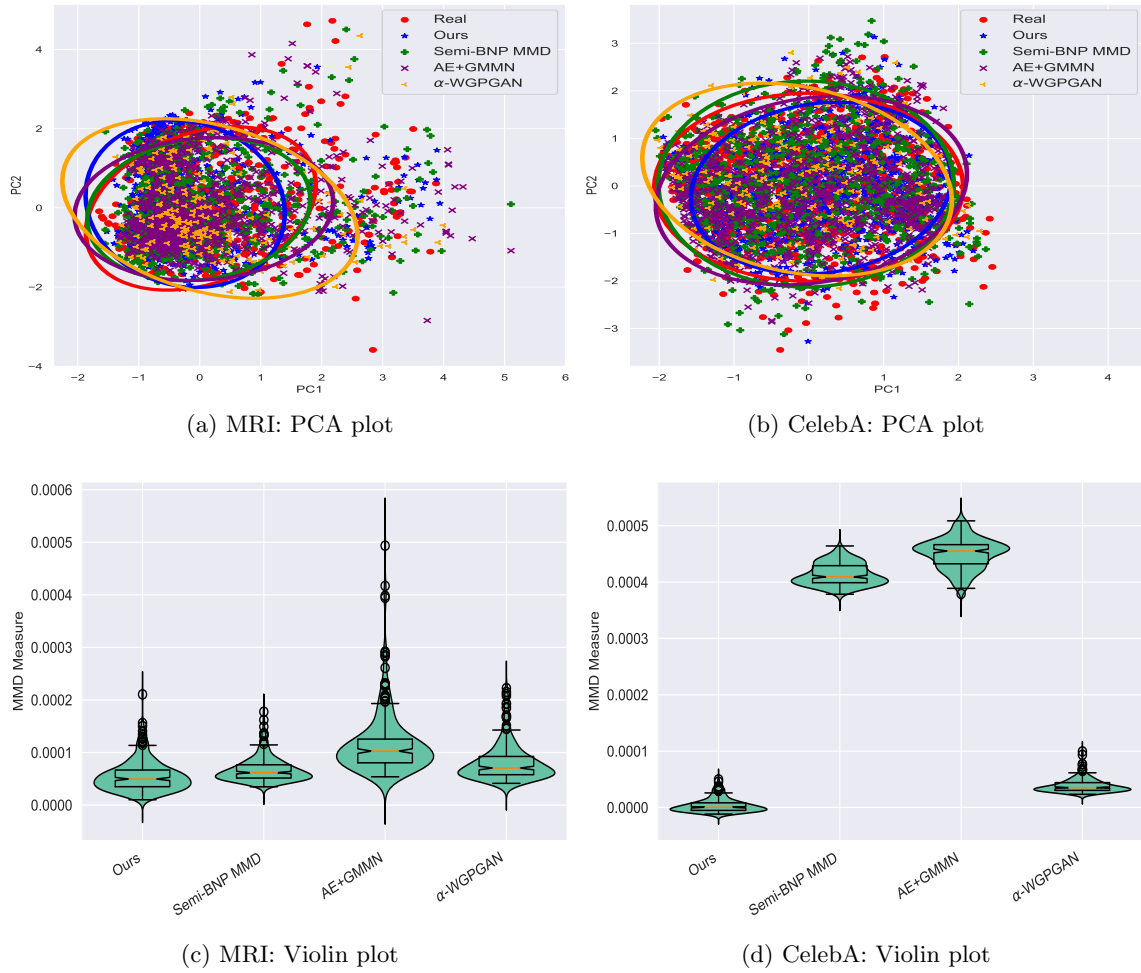
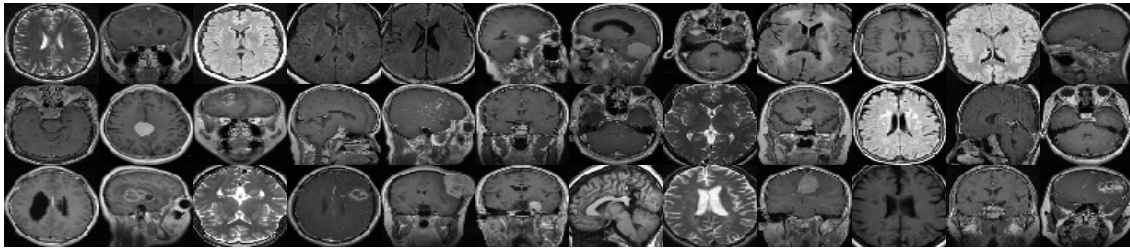
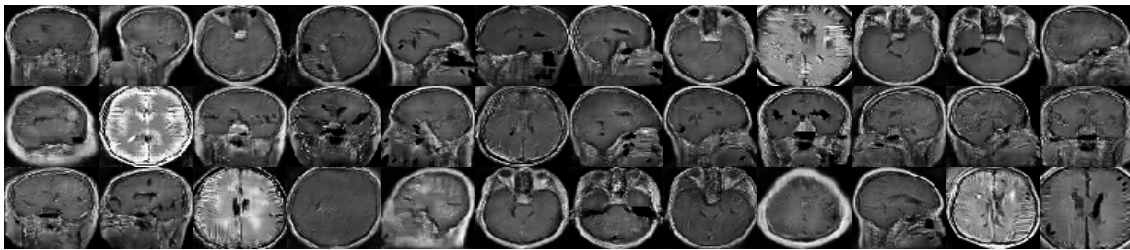


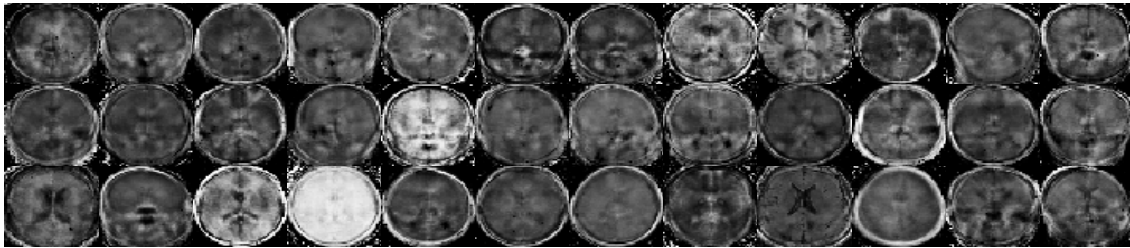
Figure 9: Top: PCA plots of 1000 generated samples versus real samples with fitted ellipse curves for MRI and celebA datasets, indicating the spread of the samples in the corresponding directions. Bottom: Violin plots of MMD scores including density and box plots.



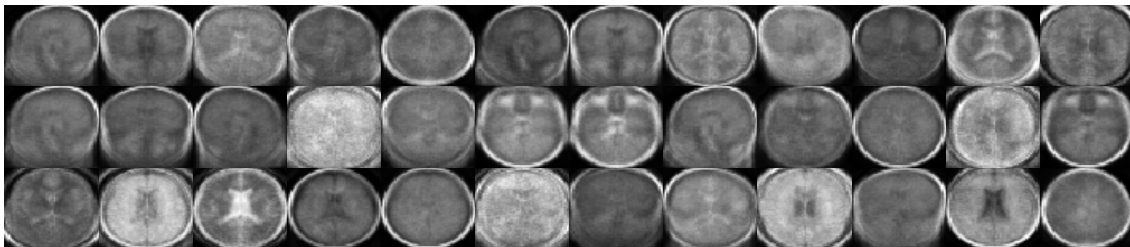
(a) Training dataset



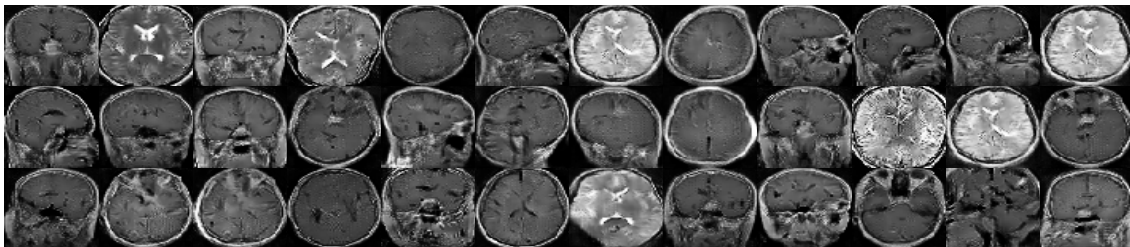
(b) Ours



(c) Semi-BNP MMD



(d) AE+GMMN



(e) α -WGPGAN

Figure 10: Visualisation of MRI training samples and generated samples using various generative models after 400000 iterations.



(a) Training dataset



(b) Ours



(c) Semi-BNP MMD



(d) AE+GMMN



(e) α -WGPGAN

Figure 11: Visualisation of celebA training samples and generated samples using various generative models after 40000 iterations.

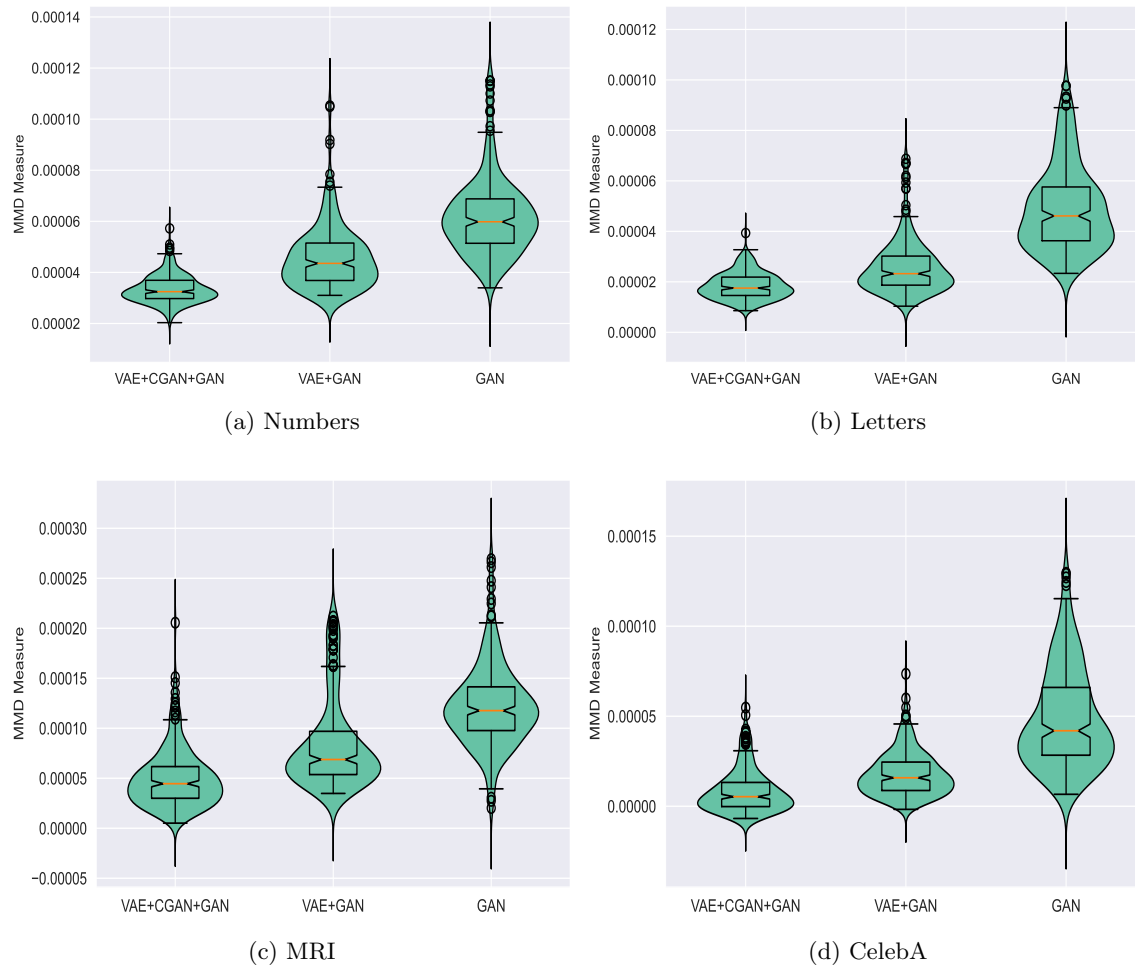
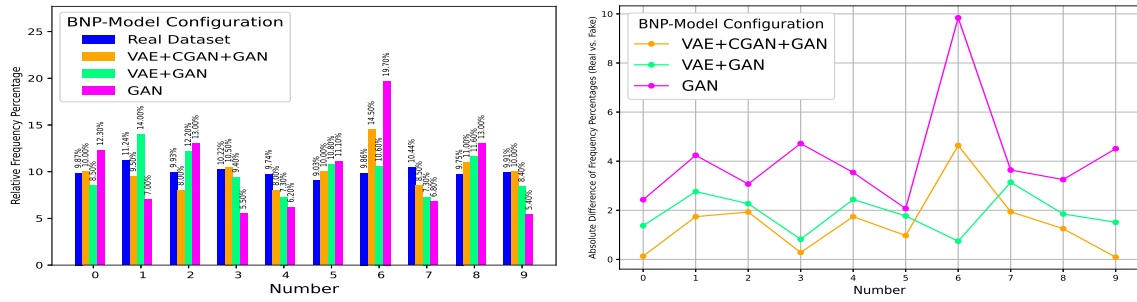
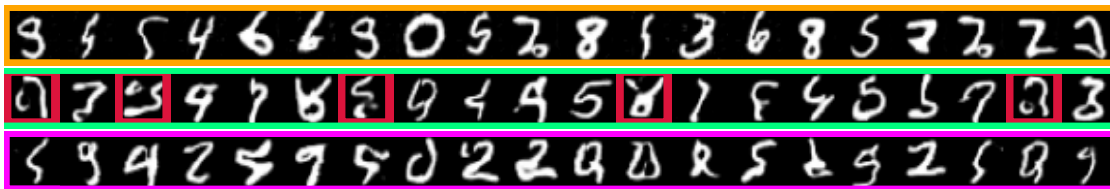


Figure 12: Comparison of MMD scores for various model configurations across datasets.



(a) Frequency Percentage

(b) Absolute Difference of Frequency Percentage



(c) Generated Samples

Figure 13: Comparison of the triple BNP model vs. partial models: The triple model—VAE+CGAN+GAN (orange)—is compared to two partial models: the dual model VAE+GAN (green) and the single model GAN (pink). All models are trained by minimizing the combined distance $WMMD(F^{pos}, F_{Gen_{\omega}})$. The top panel shows statistical analysis on 1000 generated samples, while the bottom panel visualizes 20 generated samples.

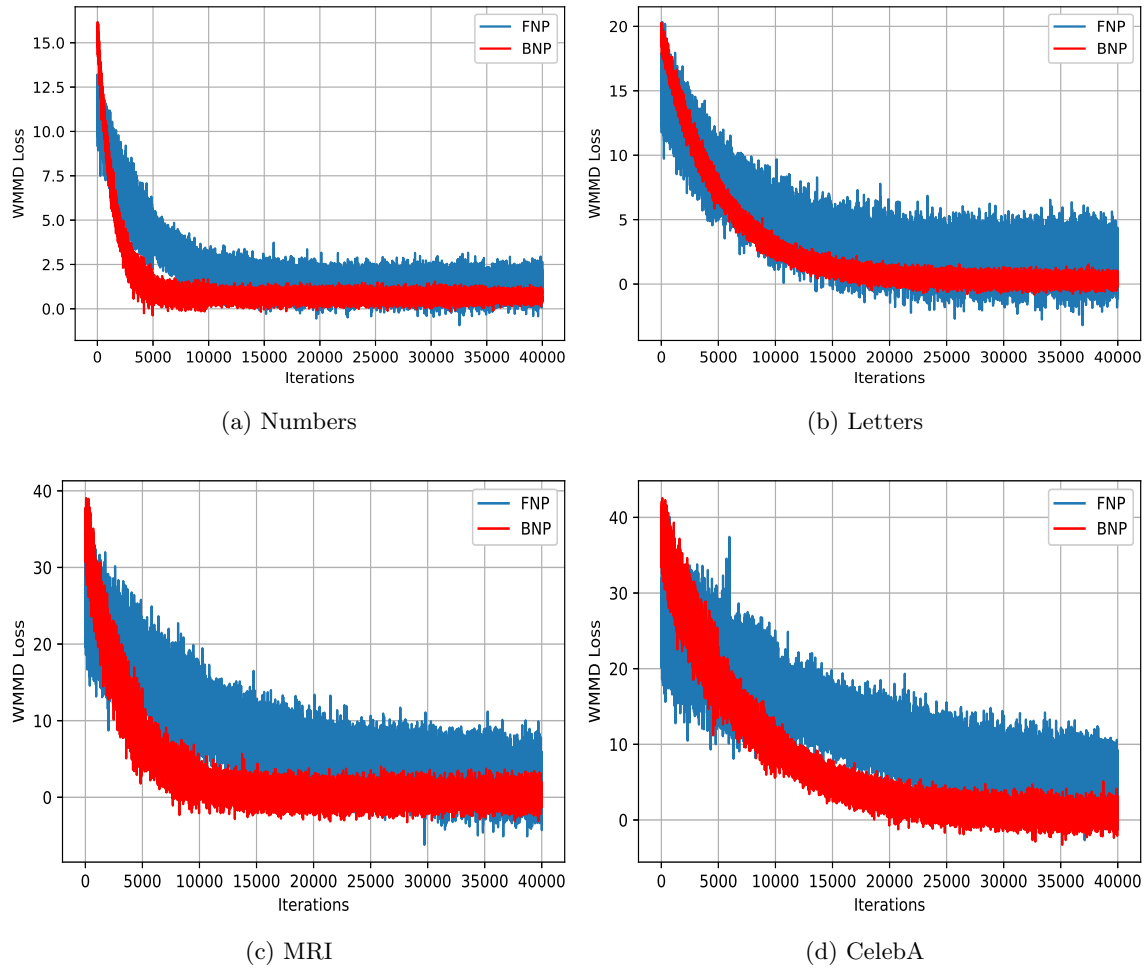


Figure 14: BNPL rate compared to the learning rate of the exact FNP counterpart, which employs resampling in computing the WMMD distance.